UCRL-18411

Cy. 2

University of California

Ernest O. Lawrence Radiation Laboratory

EXCHANGE AMPLITUDE CONTRIBUTIONS TO THE REACTION $K^- + p \rightarrow \Lambda + \pi^0$ NEAR 1 BeV/c

James Louie
(Ph.D. Thesis)

August 1968

E, P

Berkeley, California

UCRL-18411
Cy. 2

DISCLAIMER

UCRL-18411

UNIVERSITY OF CALIFORNIA

Lawrence Radiation Laboratory

Berkeley, California

AEC Contract No. W-7405-eng-48

EXCHANGE AMPLITUDE CONTRIBUTIONS TO THE REACTION $K^- + p \to \Lambda + \pi^0$ NEAR 1 BeV/c

James Louie

(Ph.D. Thesis)

August 1968

EXCHANGE AMPLITUDE CONTRIBUTIONS TO THE REACTION $K^- + p \rightarrow \Lambda + \pi^0$ NEAR 1 BEV/C

Contents

EXCHANGE AMPLITUDE CONTRIBUTIONS TO THE REACTION $K^- + p \rightarrow \Lambda + \pi^0$ NEAR 1 BEV/C

James Louie

Lawrence Radiation Laboratory
University of California
Berkeley, California

August 1968

ABSTRACT

We analyze the reaction $K^- + p \rightarrow \Lambda + \pi^0$ in terms of direct channel resonances and background exchange amplitudes, making fits to our experimental angular distributions, Λ polarizations, and $\Lambda\pi^0$ cross sections over the center-of-mass energy range 1700 to 1850 MeV. The primary aim of the study is to investigate the nature of the background terms, using K^* and nucleon crossed-channel exchanges, in the scattering amplitude required to fit our data. We confirm previous J^P assignments for $Y_1^*(1660)$, $Y_1^*(1770)$, and $Y_1^*(2030)$, and present branching ratio products $x_{\bar{K}N} x_{\Lambda\pi}$ for these three resonances. A mass and width for $Y_1^*(1770)$ are also determined. Our data do not show much sensitivity to the presence of $Y_1^*(1910)$. The assumption of simple background exchange terms alone does not seem to be sufficient to fit the data. Modifications to these terms are made, producing reasonable fits. Effects due to the assumptions of the absorption model are also considered.

I. INTRODUCTION

This thesis is part of a general study of K^- meson-nucleon interactions for incident K^- laboratory momenta between 820 and 1120 MeV/c, corresponding to KN center-of-mass energies in the range 1700 to 1850 MeV. The original motivation for the study was the discovery[1] of the "Kerth bump", a broad, asymmetric rise in the K^-p total cross section near 1 BeV/c. By comparing the total K^-p and K^-n cross sections, the isotopic-spin I=0 resonance $Y_0^*(1815)$ was advanced to explain most of the rise. However, the existence of the low momentum tail in the bump indicated a structure more complex than a single resonance, and, in studying the K^-p mass distribution in the reaction $K^-n \rightarrow K^-\pi^-p$, Barbaro-Galtieri et al.[2] suggested the presence of the $Y_1^*(1765)$. Their I=1 assignment came from analyzing interference effects in the elastic (K^-p) and charge-exchange $(\bar{K}^0n)$ angular distributions and polarizations from the earlier work of others.[3]

The present paper describes an attempt to understand some of the details of what takes place in a specific interaction in this energy region, $K^- + p \rightarrow \Lambda + \pi^0$. We found a total of some 21 000 events consisting of a beam track which disappeared with an associated charged decay of a neutral particle. After applying various criteria and kinematic analysis, there remained 7735 $\bar{K}^0$ events $(K_1^0 \rightarrow \pi^- + \pi^+)$ and 6266 weighted events representing $K^- + p \rightarrow \Lambda + \pi^0$, $\Lambda \rightarrow \pi^- + p$.

Because the $\Lambda\pi^0$ final state has I=1, any intermediate resonant state must have this same quantum number, restricting possible candidates to Y_1^*'s. In a partial-wave analysis in the same energy region of the related reaction $K^- + n \rightarrow \Lambda + \pi^-$, which has pure I=1 in both initial and final states, Smart[4] found that three Y_1^*'s and four constant background amplitudes gave a fit to his data of order 2%. By allowing a moderate energy dependence for the background, the probability of fit

increased to 8%.

The angular distribution of π^0 in the K^-p center-of-mass for $K^- + p \rightarrow \Lambda + \pi^0$ shows peaking in both the forward and backward directions suggesting possible contributions from particle exchanges in the crossed (t- and u-) channels. We have parameterized our background amplitudes by such processes, along with direct channel Y_1^* resonances. The validity of such a parameterization will be tested by comparing its predictions with our experimental data.

In Section II we discuss briefly general experimental procedures, including the properties of the beam, and the scanning and measuring of events. Section III considers the treatment of the data in selecting out the reaction of interest. We present the mathematical structure of our model in Section IV, and the comparison with the experimental data is contained in Section V. Section VI discusses the various solutions and implications of the results.

II. PRELIMINARY PROCEDURES

In this section we discuss how the K^- + p collision is effected, what events were looked for and how they were measured, the beam normalization, contamination, and attenuation.

A. Beam

A new beam using two stages of electromagnetic separation for K^- mesons was built and operated at the Lawrence Radiation Laboratory's Bevatron and directed into the 25-inch bubble chamber filled with hydrogen. Fig. 1 is a schematic of the beam line. The external proton beam impinges upon a copper target T, producing the K^- flux used in this experiment. Having a target external to the accelerator allows the selection of positive or negative particles within a wide range of momenta, since the beam is independent of the Bevatron's magnetic field. The beam was designed so that the K^- mesons are produced at 0°, the acceptance solid angle is relatively large, and a short target-to-chamber distance reduces the number of K^- lost due to decays. The beam line components, consisting of nine quadrupole magnets Q1-Q9, four bending magnets M1-M4, two mass-separation slits and a uranium collimator in addition to the two parallel plate velocity spectrometers S1 and S2, reduced the contamination (see Section D below) of non-K^- particles at the chamber to about 5% at the seven beam momenta below 1020 MeV/c, and to 9% at the two highest momenta. The magnets act as focusing elements, and the other components filter out non-K^- particles. The total momentum bite was 2%, and the horizontal width of the beam matched the entrance window at the bubble chamber, with the beam tracks entering parallel to each other. A more complete description of the beam is reported elsewhere.[5]

The nine incident laboratory (lab) momenta had nominal values between

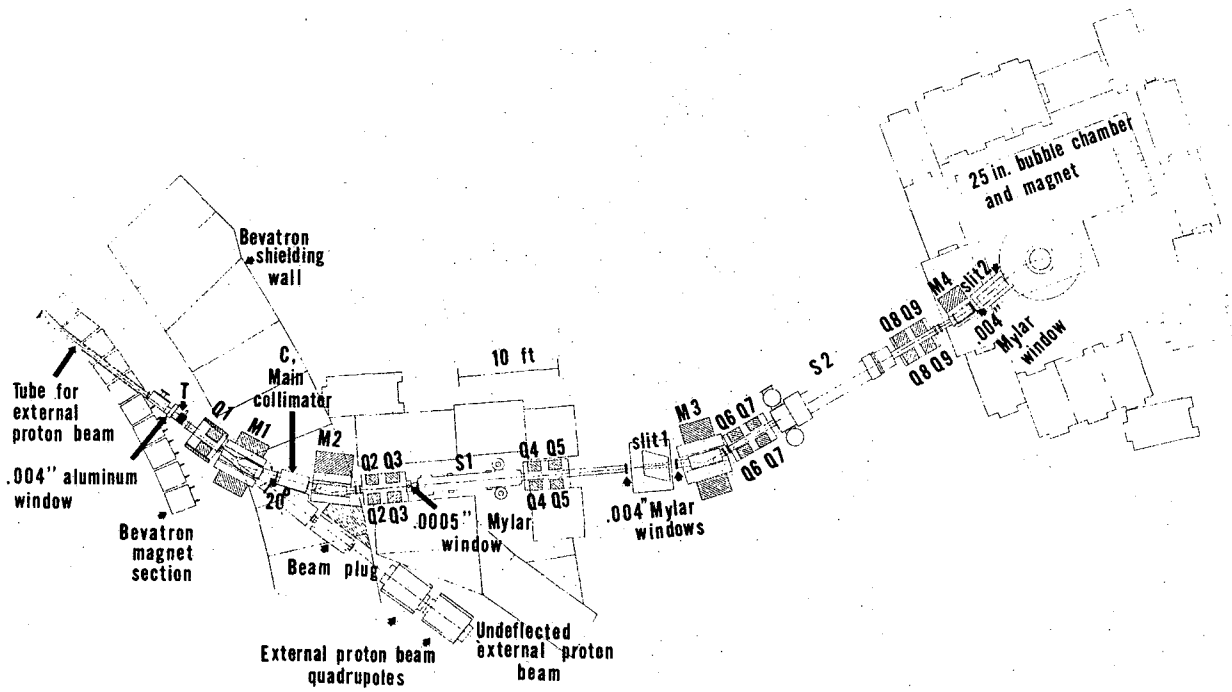

MUB-3362

Fig. 1

850 and 1150 MeV/c, representing center-of-mass (c.m.) energies between 1700 and 1850 MeV. The actual average values of the momenta, the first entry in Table I, were determined by measuring beam tracks.

B. Scanning, Measuring, and Data Reduction

The topology scanned for in this experiment, as seen in the bubble chamber, appears as a vanishing beam track with a V-like decay pointing back to the production vertex (0-prong+V) (Fig. 2). There were 144 rolls exposed for 233 000 3-view stereo pictures for the nine energies, with all of the film being scanned twice. No scanner re-examined the same roll. The initial scan had a mean efficiency of 92.9%, the second, 96.2%. Discrepancies between the two scans were resolved and new events were measured. The mean efficiency for the combined scans was over 99%.

Events found were measured on either the "FSD" (Flying Spot Digitizer) or on a "Franckenstein" machine.[6] After finding an event on the FSD scan table, a "road" is made along each track associated with the event by marking the coordinates of a point near the beginning, middle and end of each track, putting this information on magnetic tape. The film is later mounted on the FSD automatic measuring machine; information on the tape restricts the FSD to the appropriate tracks to be measured. The Franckenstein is a motor-driven, semi-automatic centering and projection microscope; measurement is accomplished by determining the coordinates of a series of points along each track associated with an event.

After measurement, the events were processed through the system of computer programs FOG-CLOUDY-FAIR written by the data handling group headed by H. S. White.[7] The events are reconstructed in three-dimensional space by FOG, finding the dip and azimuthal angles of each track as well

Table I. Summary of the beam.

1.	Beam momentum (MeV/c)	821	878	888	923	946	975	1019	1057	1112
2.	Number of good frames ($\times 10^3$)	8.62	18.23	12.83	41.46	10.27	47.40	42.76	26.41	22.58
3.	Corrected number of beam tracks ($\times 10^4$)	9.16	20.49	11.49	61.54	10.17	65.81	72.19	30.58	25.51
4.	Contamination (%)	4.9	5.0	6.3	6.0	6.6	6.0	5.3	9.3	9.2
5.	Number of K^- ($\times 10^4$)	8.71	19.46	10.76	57.85	9.50	61.86	68.36	27.77	23.16
6.	K^- path length ($\times 10^6$) (cm)	2.74	6.13	3.39	18.19	2.99	19.45	21.45	8.72	7.30
7.	Cross section/event (μb)	9.97 ±0.50	4.46 0.22	8.06 0.40	1.50 0.08	9.14 0.46	1.40 0.07	1.27 0.06	3.13 0.16	3.74 0.19

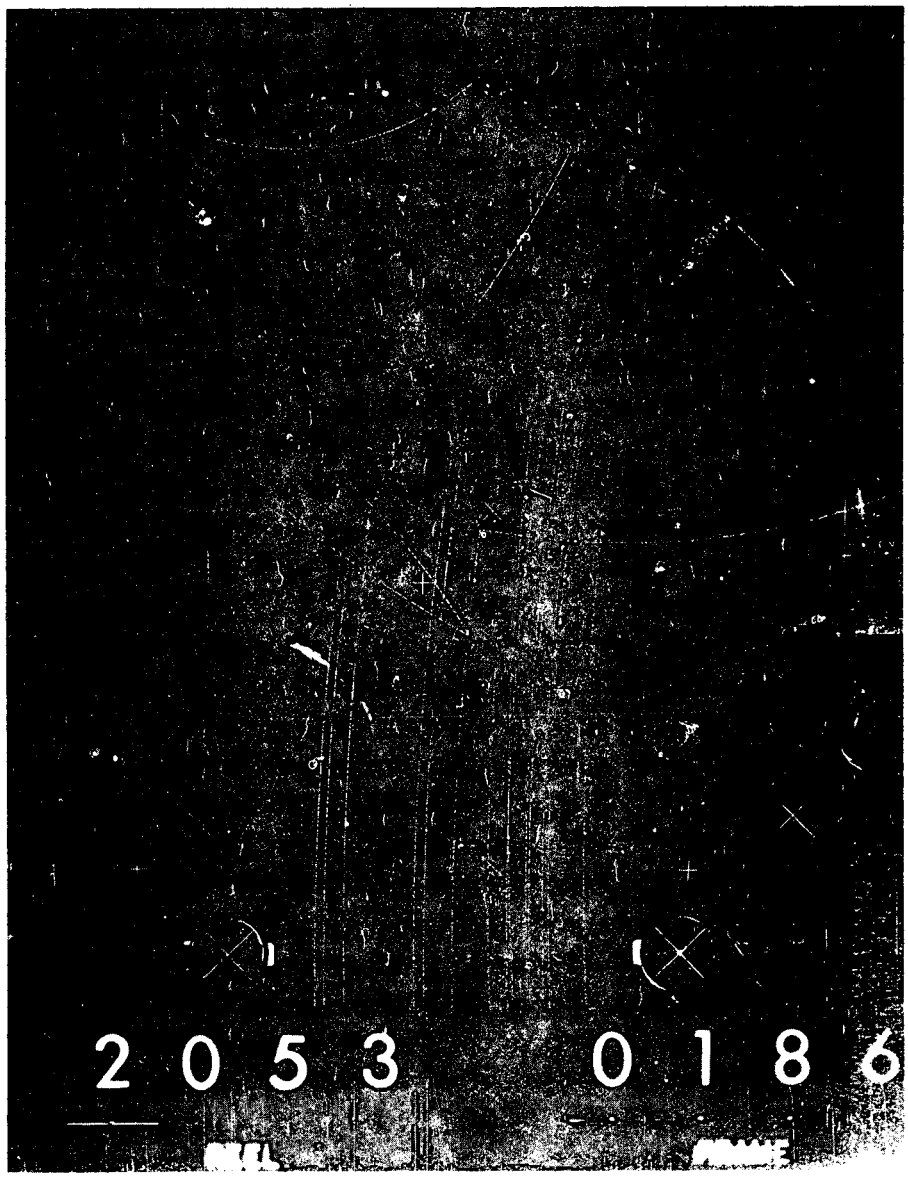

XBB 687-4005

Fig. 2

as the momentum. The errors on these quantities are calculated in CLOUDY. The reconstructed event is kinematically constrained to different hypotheses, and a χ^2 goodness-of-fit is calculated. FAIR provides the results of the computations in various forms, including page output, histograms, and scatter plots. Most of the analysis was made using data tapes put out by FAIR.

C. Beam Normalization

Path lengths are commonly determined by counting all τ decays ($K^- \rightarrow \pi^- \pi^- \pi^+$) within a certain fiducial volume, using the known branching ratio into this mode. Conversely, one can calculate this branching ratio if the numbers of τ's and K^- mesons are known. Early in the experiment, approximately 800 τ's were counted in addition to beam tracks in about 20 rolls of film, and the branching ratio turned out to be too low by about three standard deviations. A check of the scanning procedure showed that a consistent fiducial volume for counting τ's was not used, and the instructions as to the topology to record were not completely clear. The results of the τ-scan were therefore difficult to interpret meaningfully[8] in terms of a beam normalization, so a careful beam count scan was initiated.

The cross section σ for a certain type of event is proportional to the ratio N_e/N_c, where N_e is the number of these events and N_c is the number of incoming beam tracks. The percentage error in σ may be expressed

$$\frac{\Delta\sigma}{\sigma} = \sqrt{\frac{1}{N_e} + \frac{1}{N_c}}$$

$$= \frac{1}{\sqrt{N_e}} \sqrt{\frac{1+f}{f}}$$

where $N_c = f N_e$ and assuming Poisson distributions for the finding of the events and the counting of the tracks. Since N_c is of the order of one hundred times N_e, the major error comes from N_e. In order not to count an unduly number of beam tracks but still keep the contribution of N_c to the error small, we can require

$$\sqrt{\frac{1+f}{f}} \approx 1.1 \text{ or } 1.2,$$

so that $f \approx 4$; i.e., for a typical roll, $N_e \approx 200$, so one should count about 800 beam tracks per roll. Since there are ten to fifteen tracks per picture, about 65 frames per roll were counted for beam tracks, or every 25th frame. To establish criteria for acceptance of tracks to be counted, beam momentum templates were constructed to take account of the four different scan table magnifications and of the five different bubble chamber magnetic fields. The magnetic field adjustments were slight, and permitted a better centering of the beam in the chamber. The acceptable angular spread corresponds to a spread at the chamber entrance window of $\pm 2^\circ$ from the central value, which includes all but 2.0 to 3.6% of the total number of beam interactions. An average trajectory for each representative roll was calculated, and the deviations of the beam tracks from this average were plotted at a reference line 24 cm downstream from the chamber window. As an example, Fig. 3 displays the deviation, Δy, for 108 tracks from three frames (A) near the beginning and three frames (B) toward the end of roll 2201, which was taken at a nominal momentum of 1 BeV/c. Tracks falling within $\Delta y = \pm 1.2$ cm were accepted to be counted. This region contains 94% of the total number of tracks reaching the reference line. The internal region $\Delta y = \pm 0.6$ cm contains 99% of all of the acceptable tracks, which implies that during the scanning, it was not necessary to make frequent decisions about marginal beam tracks.

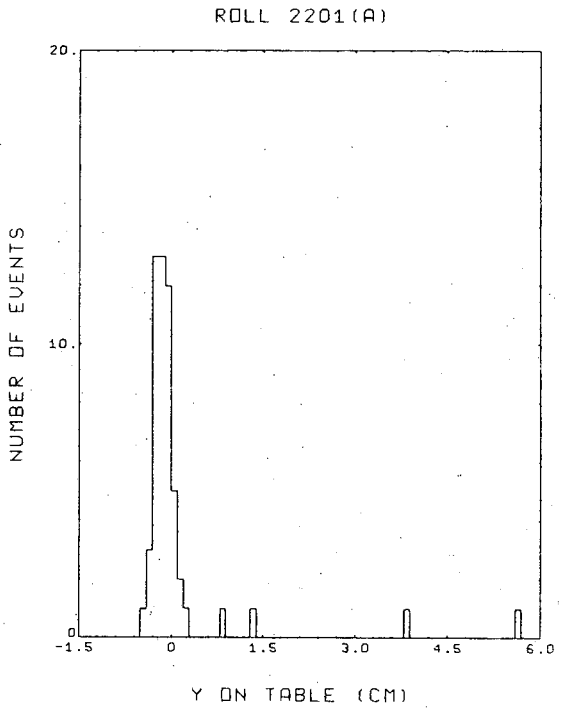

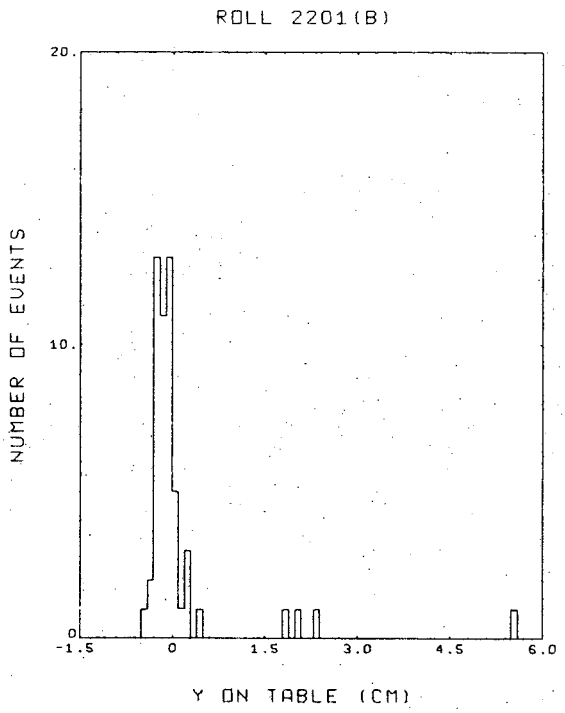

XBL 686-1063

Fig. 3

Of the 233 785 triads in the experiment, 1.6% represent "bad" pictures; i.e., they are completely dark, missing, blank, or of otherwise defective quality, and not considered further. Four per cent of the remainder, the second entry in Table I, were counted for beam tracks. Two of the rolls were checked for scanner efficiency, which was 99.2%. A particular effort was made to detect superimposed tracks. On the higher flux film, six pairs of such tracks were found, out of a total of some 800 tracks counted on the roll. The correction for beam counting efficiency constitutes a factor of 1.01 by which to multiply the number of tracks counted, and the result appears in Table I as the third entry.

D. Beam Contamination and Attenuation

The contamination of the beam due to the presence of pions and muons was estimated by counting delta rays, which result from elastic collisions between incident particles and atomic electrons. For example, the maximum kinetic energy that a 1 BeV/c K^- meson can transfer to an electron is 4 MeV, so all delta rays of a higher energy are due to less massive incident particles. This energy cut off was calculated for each momentum, and was translated into a delta ray cut off diameter for the given chamber magnetic field and for each scan table. The cross section for delta ray production by a pion or a muon was taken from Rossi,[9] and the hydrogen density in the chamber was[10] 0.0608 gm/cc. Using these quantities, the mean free path for a delta ray to be produced could be calculated. The total non-K^- meson path length is the mean free path times the number of delta rays greater than the cut off diameter, and the number of pions or muons in the beam is then the total path length divided by one track length. The exposure of film at a particular momentum usually took place during intervals of time separated by days or weeks. As far as

possible, the rolls scanned for delta rays were selected from each of these intervals, so that the approximately 20% of the total film scanned should be representative of the entire experiment. The templates used for beam track counting were also used for delta ray counting. More than one delta ray on a track was noted, as well as interactions on those tracks for which the delta ray diameter was greater than the cut off. A total of 17 interactions was found for all of the momenta. Based on an estimated total pion-proton cross section of 35 mb in this region, one expects 15% of the total of 2303 delta rays counted to be due to pions, with the rest due to muons. The total non-K^- contamination was about 5% at the seven lowest momenta and 9% at the two highest. The contamination and the actual number of K^- in the beam appear in Table I.

The beam count includes tracks which show an interaction (a collision or a decay) before reaching the reference line, as long as the angular spread criterion is met. A correction due to these depletion processes was made, and this reduction turned out to be approximately 5% over the momentum range. The corrected total K^- path length L appears in Table I, along with the cross section for one interaction, $\sigma = 1/N_A \rho L$, where $N_A \rho$ is the number of protons/cc in the bubble chamber. The total cross section for a particular reaction is determined by multiplying this σ by the number of events found. The quoted normalization error in σ is discussed below.

E. Normalization Errors

The errors in the calculation of the cross sections and mean free paths for delta ray production are small compared to other errors present in the beam normalization. The percentage errors in the calculation of the number of beam tracks, based on the number counted at each momentum,

vary from 0.5-1.5%. The errors in the calculation of the contamination arise primarily from the uncertainty in finding the number of non-K^- mesons present; i.e., from counting delta rays. These errors are in the range 5-13%. The standard deviations in finding the average contamination at each momentum are higher, with a maximum of about 30%. However, these are percentages of small quantities; the contamination itself is in the 5-10% range. Hence the combined error in finding the number of K^- in the beam is at the 2% level, and when we take account of the errors in the attenuation and beam count efficiency calculations, both in the 1-2% range, the normalization error is about 3%. However, we use an error of 5% in Table I to try to account as well for additional uncertainties such as the actual ratio of pions to muons in the contamination and the actual hydrogen density.

When properly done, it is less tedious to find the beam normalization by counting τ's, using the known branching ratio for this decay. A τ-count was later undertaken,[8] yielding some three hundred τ's at each of the various momenta. If one were to normalize using τ's, the percentage errors would be at the 5-6% level, compared to an estimated maximum of 5% by doing a beam count. Hence the beam count scan, while lengthier, gives more accurate results.

III. DATA ANALYSIS

Here we discuss the identification of the reactions, kinematic and fiducial selection criteria to eliminate biases, and weighting for events missed or unmeasured to obtain our final sample of events.

A. Kinematic Fitting

The 0-prong+V topology can be the result of any of the reactions

$$
\begin{array}{lll}
K^- + p \rightarrow \Lambda + \pi^0 & & \\
\quad \rightarrow \Lambda + (c\pi^0),\ c > 1 & & \\
\quad \rightarrow \Lambda + \eta & & \\
\quad \rightarrow \Sigma^0 + \pi^0 & \Sigma^0 \rightarrow \Lambda + \gamma & \\
\quad \rightarrow \Sigma^0 + (c\pi^0),\ c > 1 & \Sigma^0 \rightarrow \Lambda + \gamma & \\
\quad \rightarrow \bar{K}^0 + n & & \\
\quad \rightarrow \bar{K}^0 + n + (c\pi^0),\ c \geq 1 & &
\end{array}
\qquad
\left.\begin{array}{l}
\\ \\ \\ \\ \\ \\ \\
\Lambda \rightarrow \pi^- + p \\ \\ \\ \\ \\
\bar{K}^0 \rightarrow \pi^- + \pi^+ \\
\bar{K}^0 \rightarrow \pi^- + \pi^+
\end{array}\right\}
\begin{array}{l}
\text{(a)} \\ \text{(b)} \\ \text{(c)} \\ \text{(d)} \\ \text{(e)} \\ \text{(f)} \\ \text{(g)}
\end{array}
\quad (1)
$$

The four equations representing conservation of energy and momentum provide the constraints at any vertex. The V, or decay vertex, was tried sucessively as $\bar{K}^0$ (K_1^0) and then as Λ. The kinematics are such that the K_1^0 can be produced at all lab angles relative to the incident K^-, including the backward direction, whereas the maximum angle for Λ production is approximately 60° at these energies. Fig. 4A is a kinematic ellipse plot for $\Lambda\pi^0$ production, and Fig. 4B is the corresponding plot for $K_1^0 n$, both drawn for an incident K^- momentum of 1019 MeV/c. Lab momenta and angles can be read off directly for various c.m. production angle cosines.

Assuming that the decaying neutral comes from a given 0-prong, or production vertex, the only unknown quantity for either hypothesis is the magnitude of the momentum of the neutral, so the event is subject to three constraints (a "3C-fit"). The hypothesis which made a better

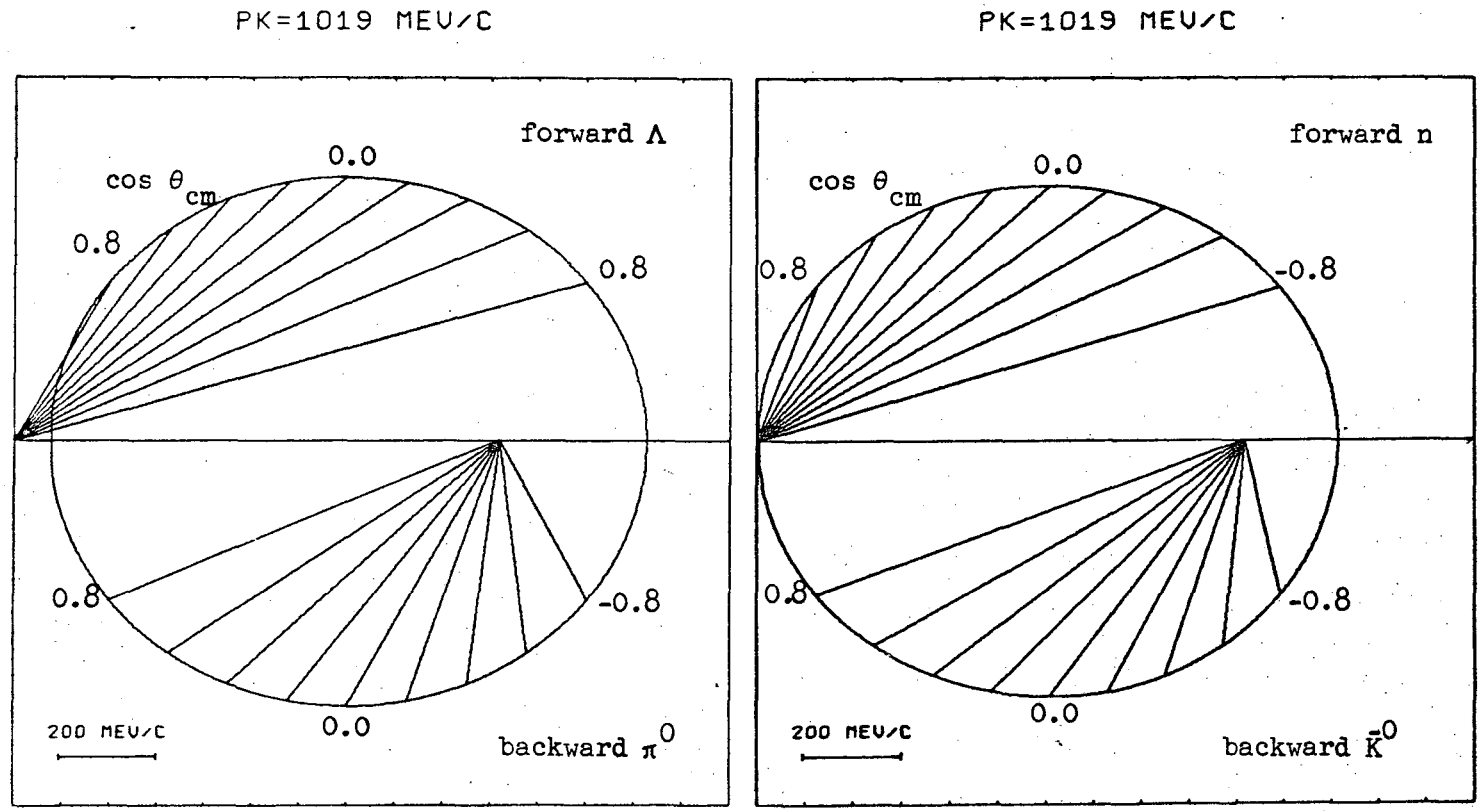

LAMBDA-PI KINEMATICS

A.

KO-NEUTRON KINEMATICS

B.

XBL 686-1135

Fig. 4

3C-fit was assumed to be correct, as the first step in the event differentiation. On occasion, in a single picture, more than one 0-prong and/or V are present. For example, if two 0-prongs and one V are seen, the V is assumed to come from either 0-prong, and two events are measured for that frame. The extra, or duplicate, events are filtered out by rejecting the one which makes a poorer 3C-fit for either K_1^0 or Λ hypothesis. About 15%, or 3659 events, of the total number of 0-prong+V's measured are duplicates.

B. Ambiguities

Some 500 of the events which fit the K_1^0 hypothesis also fit the Λ hypothesis. This confusion can arise when the lab momenta of the decay products and the decay opening angle for the two cases are identical. The kinematics for the two decays are such that for any opening angle, the positively charged particle will have about ten times the momentum of the negatively charged particle at these points of confusion. Fig. 5A displays curves of constant decay opening angle between the decay products for K_1^0 and Λ; the lab momentum of the negatively charged decay product is plotted against that of the positively charged product. The region near an intersection of two curves for the same angle produces the situation described. It is possible to resolve the ambiguity by observing that, at these points, the π^- in the K_1^0 c.m. always falls near the backward direction when referred to the K_1^0 lab momentum. Since the expected π^- distribution in the K_1^0 c.m. is isotropic, the extra events from confusing Λ decays show up clearly in the backward angles; Fig. 5B is a histogram of this π^- distribution. All of the events for which $-1 \leq \cos(\pi^-, K_1^0) \leq -0.8$, in the K_1^0 c.m., were examined on the scan table and identified by means of ionization estimates (density of tracks). Of 1020 events

A.

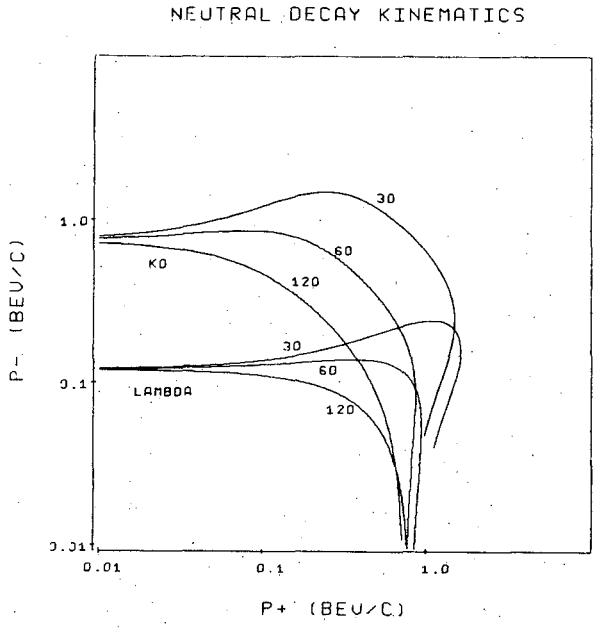

B.

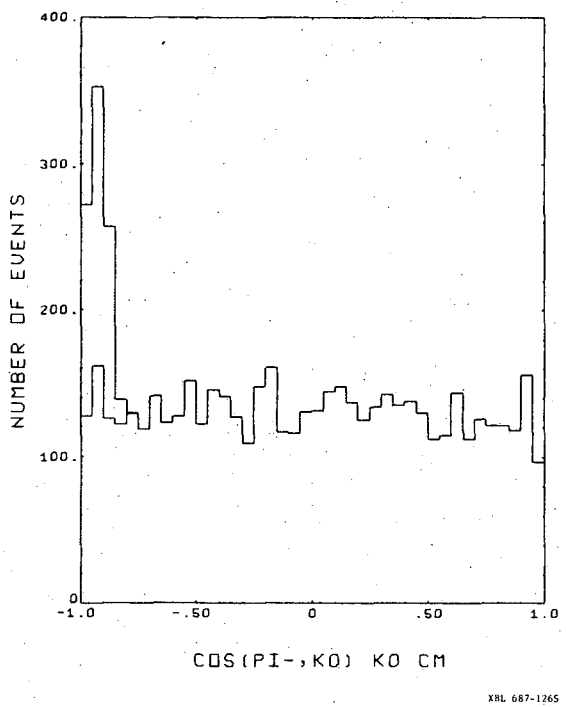

XBL 687-1265

Fig. 5

surviving the fiducial and length criteria (see Section C below), 523 were identified as K_1^0 decays and 485 as Λ, with 12 as neither. These latter 12 events are elastic scatters, from non-beam tracks, or otherwise misidentified, and therefore rejected. After the resolution of this ambiguity, there were 13 577 Λ events and 7735 K_1^0 events. Further analysis involves primarily these Λ events, the subject of this paper.

C. Fiducial Volume Criteria

Near the edges of the chamber, because of poorer illumination, lower scanner efficiency, less accurate measurement of tracks, and a high probability of the Λ decaying outside the chamber and hence being unmeasurable, two fiducial volumes were imposed. Beam tracks not interacting in the first 38 cm of the chamber were rejected, and acceptable events had to have the K^- travelling at least 5 cm into the chamber. Because of the slight curvature of the beam tracks in the magnetic field, we actually used a value of 33.1 cm rather than 33 cm for the total K^- track length determination in Table I. Also, the decay vertex had to be located within a cylinder of radius 21.5 cm and height 15 cm and centered 24.5 cm from the entrance window, which allowed about 6 cm for the measurement of the decay products. Fig. 6A shows the positions of the production vertex along the chamber, where x=29 cm is the position 5 cm into the chamber. Fig. 6B is a plot of the lateral position of the decay vertices along the beam; the cylinder described above is located at (x,y)=(48.5,50) cm. These two criteria eliminated 12% of the Λ's.

D. Weighting for Length Cuts

Events were rejected because of certain kinematic criteria, and were compensated for by appropriate weighting. Some of the Λ's are

A.

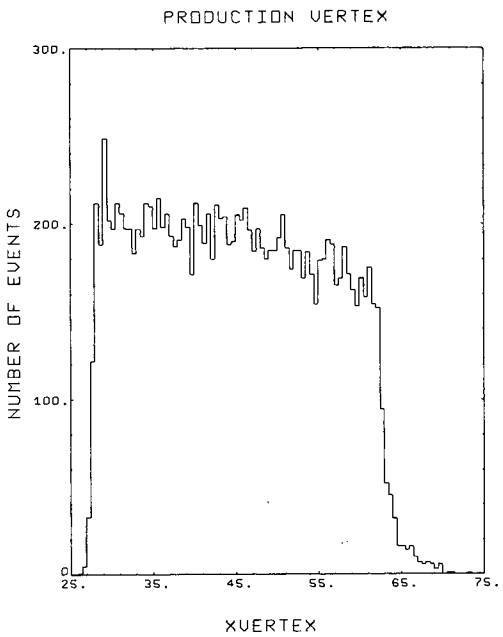

B.

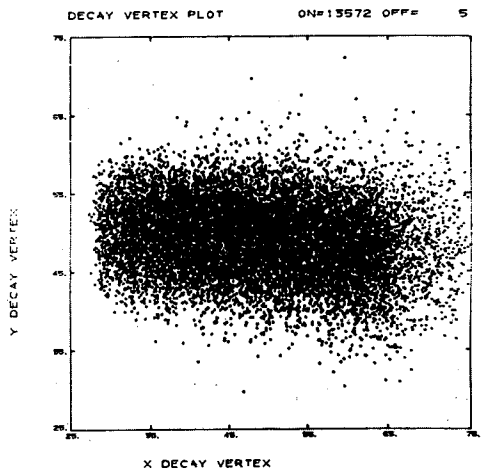

XBB 687-4007

Fig. 6

missed because the decay takes place (a) outside the chamber or very near to its walls, or (b) very close to the production vertex. There is then an interval $[L_o, L_p]$ in which the decay length has to be in order that the decay can be recognized and measured. L_o is the cut off length and L_p is the potential length, defined as the distance between the point of production and the surface of the cylinder used for the fiducial volume of the decay vertex, described above in Section C. The Λ's decay exponentially, so the probability that the decay is measurable is given by

$$P_L\ (L_o < L < L_p) = \exp\ (-L_o/d) - \exp\ (-L_p/d).$$

If τ is the mean life of the Λ, its mean length d is given by $d=c\tau p_\Lambda/m_\Lambda$, where the constant $c\tau$ is taken to be 7.61 cm, based on[11] $\tau=(2.52 \pm 0.04) \times 10^{-10}$ sec. m_Λ is the mass of the Λ in BeV, and its momentum p_Λ is in BeV/c. The actual number of Λ's is then found by multiplying each event with a decay length in the interval $[L_o, L_p]$ by its weight W_L, defined to be the inverse of the probability that the event is measurable; i.e., $W_L=1/P_L$. Fig. 7A is a histogram of the length of the Λ for intervals of 0.2 cm. The cut off length L_o was taken to be 0.8 cm and eliminated 13% of the events remaining after the fiducial criteria were met and before weighting. A histogram of W_L is shown in Fig. 7B for events meeting fiducial and length criteria and satisfying the selection in the square of the missing mass (see below). The average W_L for the final $\Lambda\pi^0$ sample was 1.33.

To insure that L_o was large enough so that steep, low energy Λ's were not missed, the following test was made. Define lab polar coordinates such that the beam direction is along the z-axis with θ the polar angle between the Λ produced and the beam direction. Let φ be the azimuthal

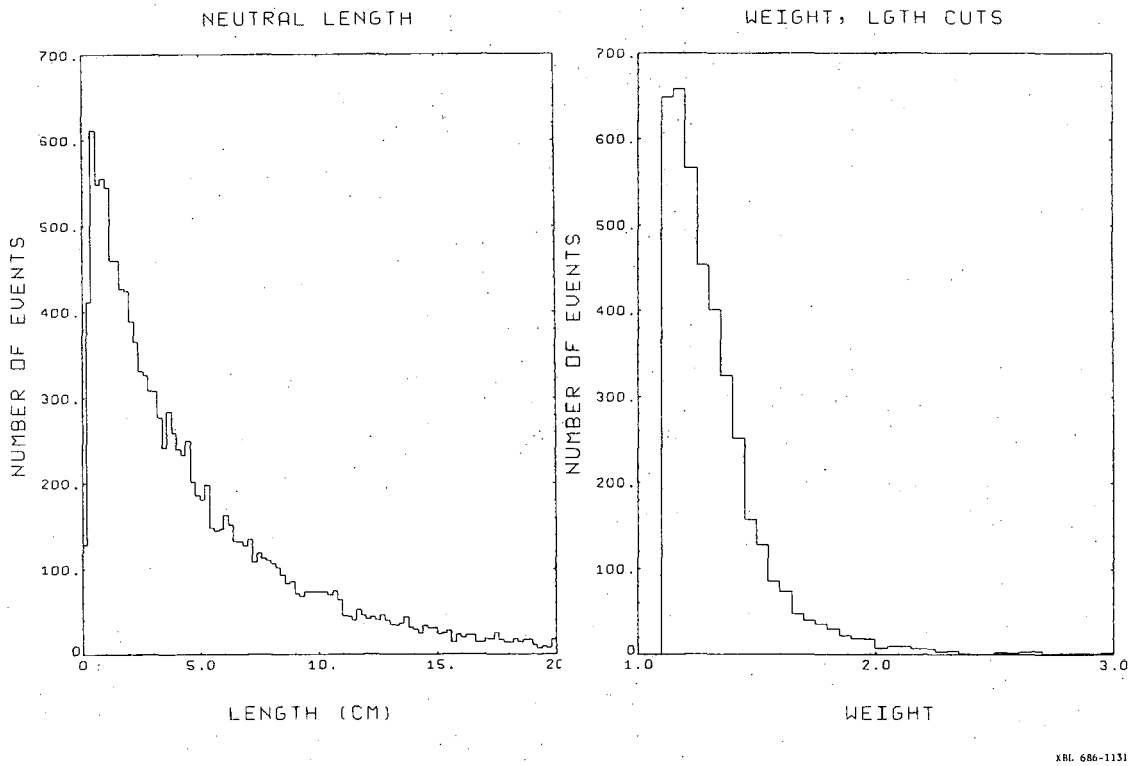
NEUTRAL LENGTH
NUMBER OF EVENTS
700.
600.
500.
400.
300.
200.
100.
0
0
5.0
10.
15.
20
LENGTH (CM)
WEIGHT, LGTH CUTS
NUMBER OF EVENTS
700.
600.
500.
400.
300.
200.
100.
0
1.0
2.0
3.0
WEIGHT
XBL 686-1131

A. B.

Fig. 7

angle, with φ=90° (270°) for $\vec{p}_\Lambda$ in the plane defined by the beam direction and the camera axis and moving away (toward) the camera. The azimuthal distribution of events should be isotropic, and events lost for steep Λ's would occur near φ=90° and 270°. Fig. 8A is a plot of this distribution for production c.m. cosines between -1 and -0.8 (high Λ momenta), and Fig. 8B is for the cosines between +0.8 and +1 (low Λ momenta). The latter distribution would be most sensitive to the effect.

As a further check to see that we did not miss low energy Λ's, we calculated the value of the Λ lifetime using the Bartlett method[12] for a sample of events satisfying fiducial, length, missing-mass-squared and χ^2(1C) less-than-ten criteria. The missing-mass-squared and 1C-fit criteria are discussed in Section E below. For this determination we computed the distance travelled by the Λ by using the FSD-measured decay vertex and a corrected production vertex. This latter position was located by extending the beam track and Λ momentum directions and finding the point of closest approach.[13] For 3950 events, our value found was $\tau=(2.51 \pm 0.05) \times 10^{-10}$ sec in excellent agreement with the world average[11] noted above.

E. Selection of the Reaction $K^- + p \rightarrow \Lambda + \pi^0$

Because of the difficulty in determining the actual location of the end of the 0-prong,[13] the 3C-fit was used only to eliminate the duplicate events and to resolve the ambiguity in the K_1^0 and Λ decay kinematics. Further analysis used kinematic quantities calculated from a 1C-fit, for which the information on the direction of the Λ from its point of production was disregarded. The three unknowns--the magnitude of the Λ momentum as well as its dip and azimuthal angles--reduce the number of constraints to one.

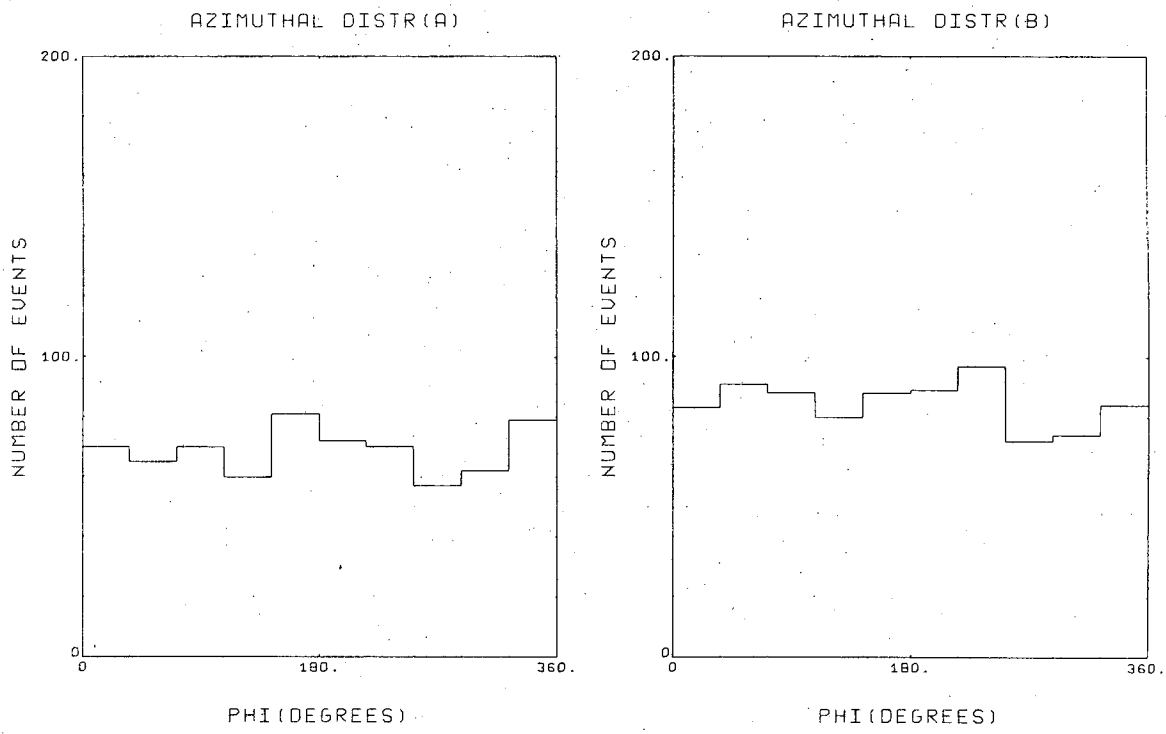
AZIMUTHAL DISTR(A)
200.
100.
0
NUMBER OF EVENTS
0
180.
360.
PHI(DEGREES)
AZIMUTHAL DISTR(B)
200.
100.
0
NUMBER OF EVENTS
0
180.
360.
PHI(DEGREES)
X8L 686-1132

A. B.

Fig. 8

The final state $\Lambda\pi^0$ is identified by examining the distribution of the square of the invariant mass, m^2, of the system of undetected neutral particles recoiling against the Λ. Fig. 9 shows the sum of the distributions for all of the momenta. The π^0 peak is prominent near 0.02 BeV^2, and the η peak can be seen at 0.3 BeV^2. Reactions of the kind $K^- + p \rightarrow \Sigma^0 + \pi^0$ followed by the rapid decay $\Sigma^0 \rightarrow \Lambda + \gamma$ and then $\Lambda \rightarrow \pi^- + p$ simulate the kinematics of, and contaminate, the reaction $K^- + p \rightarrow \Lambda + \pi^0$, $\Lambda \rightarrow \pi^- + p$. To extract a relatively pure sample, we considered the following. A simple minimum requirement for χ^2 was insufficient, since an event which had a value of m^2 far from $m_{\pi^0}{}^2$, the square of the π^0 mass, would be acceptable if its error in m^2 was large as well. This would admit Λ+(multiple π^0) states also. On the other hand, requiring m^2 to be within a certain range of $m_{\pi^0}{}^2$ alone would eliminate legitimate $\Lambda\pi^0$ events when the error in m^2 happened to be large. It can be shown that the error in m^2 is large for large values of the Λ momentum, and such a restriction in m^2 would deplete the angular distributions in the regions of large p_Λ; i.e., in the backward c.m. production cosines (see Fig. 4A). To avoid this bias while making a selection in m^2, we weighted each event which passed by $W_m = 1/P_m$, where P_m is the probability which m^2 has of falling within an interval $\Delta \equiv \Delta m^2$ from $m_{\pi^0}{}^2$. Assuming Gaussian distributed measurements,

$$P_m\,(m^2 - m_{\pi^0}{}^2 < \Delta) = \frac{1}{\sqrt{2\pi}\,e} \int_{m_{\pi^0}{}^2-\Delta}^{m_{\pi^0}{}^2+\Delta} \exp\left\{-\frac{(m^2 - m_{\pi^0}{}^2)^2}{2\,e^2}\right\} dm^2$$

$$= \frac{2}{\sqrt{\pi}} \int_0^{\Delta/\sqrt{2}\,e} \exp\,(-y^2)\,dy,$$

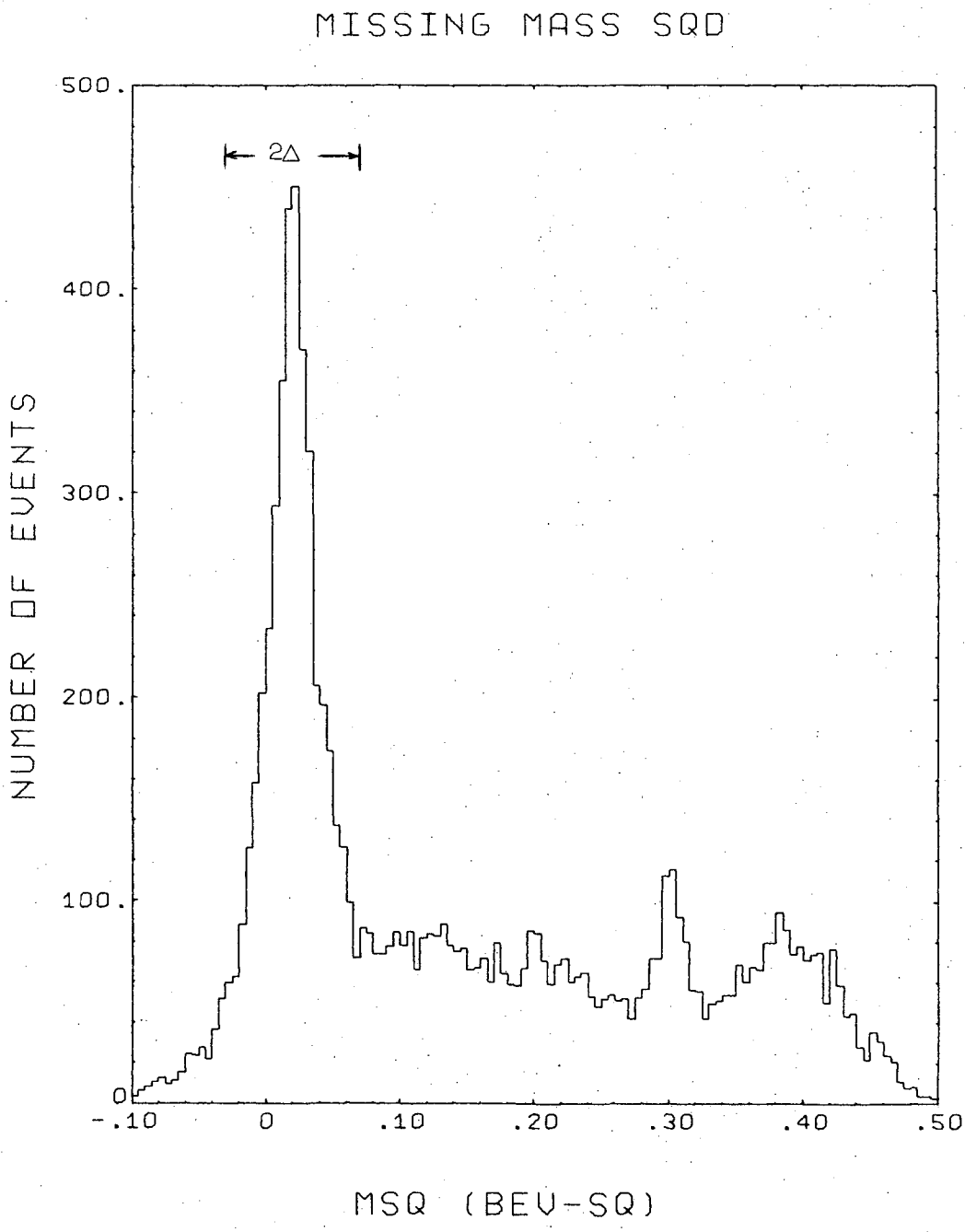

XBL 686-1129

Fig. 9

where e is the error in m^2 and $y^2=(m^2-m_{\pi^0}{}^2)/2e^2$. The latter form was used for convenience in programming. We set $\Delta=0.05$ BeV^2, since just above this point, a missing mass equal to that of two π^0 becomes kinematically possible. The angular distribution for this selection in m^2, before and after weighting by W_m, is shown in Fig. 10A. It is apparent that the weighting restores $\Lambda\pi^0$ events in the backward directions. The average weight was $W_m=1.16$, and for our final selection of events, we also required $\chi^2 < 10$ for the 1C-fit (see Fig. 10B). Each event which passed all of the selection criteria was weighted by $W=W_L W_m$, where W_L is defined in Section D.

The theoretical m^2 spectrum for the $\Sigma^0\pi^0$ final state $(\Lambda+(\pi^0\gamma))$ is flat because the Σ has spin $\frac{1}{2}$; this spectrum ranges from $m^2 \approx m_{\pi^0}{}^2$ up to a value dependent upon the c.m. energy. For example, for a 1 BeV/c incident K^- lab momentum, $m_{max}{}^2 \approx 0.27$ BeV^2. From an examination of the deviation from symmetry at the $m_{\pi^0}{}^2$ position, there still remains, after all selection criteria have been met, an estimated 5% contamination from $\Sigma^0\pi^0$. A summary of the various selection criteria is given in Table II.

A.

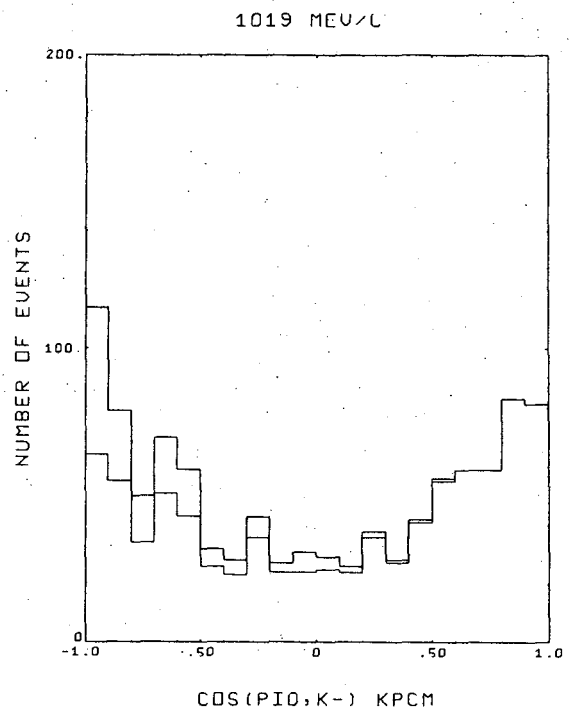
1019 MEV/C
200.
100.
0
NUMBER OF EVENTS
-1.0
.50
0
.50
1.0
COS(PIO,K-) KPCM

B.

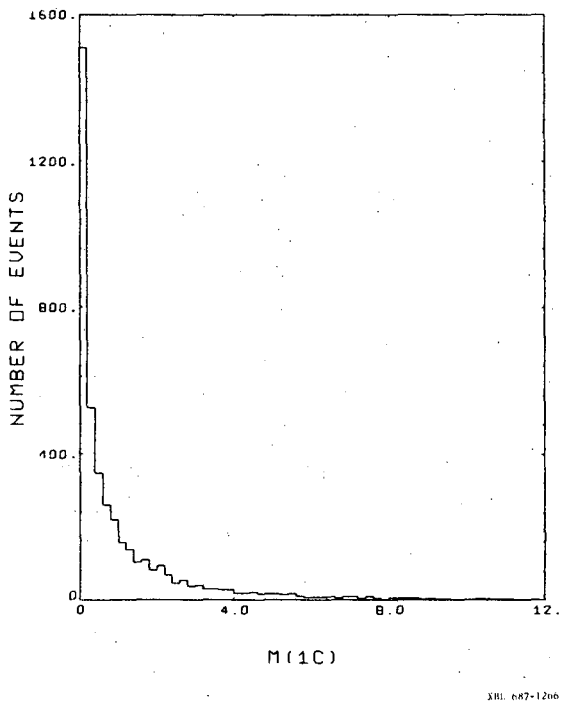
1600.
1200.
800.
400.
0
NUMBER OF EVENTS
0
4.0
8.0
12.
M(1C)

Fig. 10

Table II. Results of selection criteria and weighting.

Beam momentum	821	878	888	923	946	975	1019	1057	1112
Number of Λ's	308	798	453	2755	512	3169	3383	1300	899
after (a)	289	729	415	2549	482	2924	3119	1189	835
after (a),(b)	283	709	405	2471	465	2822	3007	1151	804
after (a)-(c)	244	629	344	2160	385	2463	2635	991	695
after (a)-(d)	232	591	326	2043	370	2330	2438	940	647
after (a)-(c),(e)	117	305	174	961	172	966	905	351	211
after (a)-(e)	113	297	171	941	171	937	875	334	207
Weighted number of Λ's									
after (a)-(d)	346	868	516	3147	593	3590	3723	1445	981
after (a)-(e)	169	444	272	1471	263	1468	1352	515	312

(a) production vertex selection
(b) decay vertex selection
(c) neutral length selection
(d) χ^2(1C) selection
(e) missing-mass-squared selection

IV. THEORETICAL BASIS AND MODEL

We analyze the reaction $K^- + p \rightarrow \Lambda + \pi^0$ by considering direct-channel resonances and crossed-channel exchanges for the background. There exist earlier studies using a similar approach for both πN and $\bar{K}N$ reactions. Several workers have considered the associated production reactions

$$\pi^- + p \rightarrow \Lambda + K^0 \qquad (2)$$

and

$$\pi^+ + p \rightarrow \Sigma^+ + K^+ \qquad (3)$$

in terms of models consisting of direct channel N and Δ resonances and background exchange terms. Hoff[14] studied (2) for incident pion momenta around 1 BeV/c, obtaining good fits to the angular distributions and polarization data by assuming a K^* -exchange along with a P1 and a narrow F5 resonance. This was an improvement over a model by Kanazawa,[15] who found reasonable fits using a nucleon pole and Σ -exchange along with P1 or P3 resonant amplitudes. At the time the K^* was undiscovered. For the same beam momentum region, Evans and Knight[16] proposed a model consisting of hyperon-and K^* -exchanges as well as P3 and F7 resonances to correctly give the qualitative trends for (3). For the same reaction, with more experimental data available, Holladay[17] constructed several models, including one using the P3 and F7 resonances with K^* - and Λ-exchange amplitudes. Fair agreement was obtained with the total and differential cross section data. The Σ^+ polarization prediction improved through the introduction of a parameter δ; because of other channels being open, Holladay multiplied the exchange contributions by $e^{i\delta}$. In addition, the energy dependence of the resonant width was parameterized differently from that of Evans and Knight.

For $\bar{K}N$ reactions, Stevenson[18] allowed D3, D5, and F7 or G7 resonances with crossed channel exchanges to obtain a χ^2/data point of 2.66 for the reaction $K^- + p \rightarrow \Lambda + \pi^0$ between 620 and 1700 MeV/c. This eleven parameter model was designed to differentiate between F7 and G7 for the then proposed Y_1^* near 2050 MeV. More recently, Minami[19] considered two Y_0^* and four Y_1^* resonances with a ρ-exchange amplitude to describe the charge exchange $K^- + p \rightarrow \bar{K}^0 + n$ near 1.6 BeV/c. A prediction for the polarization of the recoil nucleon is given, but experimental data were unavailable for comparison.

As noted in the introduction, the c.m. production angular distributions show peaking in both the forward and backward directions for $K^- + p \rightarrow \Lambda + \pi^0$ in our energy region, suggesting t- and u-channel exchange amplitudes. The intermediate valley moves slowly from the forward to the backward region as the energy increases, and the forward peak begins to turn over at the highest momenta. The backward peak, however, persists. Our approach, with precedents noted above, consists in constructing a model using known Y_1^* resonances in and near our energy region along with background crossed channel exchanges. The resonant partial waves are characterized by the Breit-Wigner form (Section B below) and we consider K^* -exchange in the t-channel and nucleon-exchange in the u-channel (Section C). We have also allowed phase factors $e^{i\varphi}$ for these exchange amplitudes, although strictly speaking, these terms should be real. Methods of analysis of two-body collisions are generally well-known,[20] and in this section we outline the mathematical framework for our model with which to compare the experimental angular distributions, polarizations, and total $\Lambda\pi^0$ cross sections. We express our equations in rather full detail, since conventions and notations in the literature show some

degree of latitude. We follow in general the conventions of Bjorken and Drell.[20]

A. Kinematic Considerations

The reaction $K^- + p \rightarrow \Lambda + \pi^0$ is an example of a meson of spin zero scattering on a baryon of spin ½. In terms of the Dirac matrices γ_μ and the spinors u_p and u_Λ for the proton and Λ, the Feynman amplitude may be written, in general,

$$F_{fi} = \bar{u}_\Lambda(p_2) \left[A + \frac{B}{2} \gamma_\mu (k_1 + k_2)_\mu \right] u_p(p_1) , \qquad (4)$$

where k_1 (k_2) and p_1 (p_2) are the four-momenta of the initial (final) meson and baryon, and A and B are functions of the total c.m. energy w and the cosine of the production angle θ between the c.m. momenta $\vec{k}_1$ and $\vec{k}_2$. The production amplitude T_{fi} may be expressed in terms of Pauli spinors and matrices,

$$T_{fi} = \chi_f^+ \left[g + h \, (\vec{\sigma} \cdot \hat{p}_2) \, (\vec{\sigma} \cdot \hat{p}_1) \right] \chi_i \ ,$$

where the amplitudes g and h are related to A and B by

$$g = C_+ \left[A + \frac{B}{2} (2w - m_1 - m_2) \right] \qquad (5a)$$

and

$$h = C_- \left[-A + \frac{B}{2} (2w + m_1 + m_2) \right] , \qquad (5b)$$

with

$$C_\pm = \left(\frac{|\vec{k}_2|}{|\vec{k}_1|} \right)^{1/2} \frac{1}{8\pi w} \left[(E_1 \pm m_1) (E_2 \pm m_2) \right]^{1/2} .$$

Here m_1 (m_2) and E_1 (E_2) are the mass and c.m. energy of the proton (Λ).

We can rewrite the operator

$$M = g + h\ (\vec{\sigma} \cdot \hat{p}_2)\ (\vec{\sigma} \cdot \hat{p}_1)$$

$$= a - i\ b\ \vec{\sigma} \cdot \vec{n} \sin\theta \quad ,$$

where

$$a = g + h \cos\theta \quad , \tag{6a}$$

$$b = h \quad , \tag{6b}$$

and the normal to the scattering plane is defined as $\vec{n}=(\vec{k}_1 x \vec{k}_2)/|\vec{k}_1 x \vec{k}_2|$. In terms of the non-spin-flip and spin-flip amplitudes a and b, the differential cross section I and polarization P_Λ of the Λ's in the $\vec{n}$ direction are

$$I = \frac{d\sigma}{d\Omega} = |a|^2 + |b|^2 \sin^2\theta \tag{7}$$

and

$$IP_\Lambda = -2 \sin\theta\ \mathrm{Im}(ab^*) \ . \tag{8}$$

The contributions to a and b in this model arise from the resonant and exchange terms discussed below. The resonant terms a_R and b_R are calculated directly. For the exchange terms, the amplitude is first calculated in the form of (4) to find A and B, and then equations (5) and (6) are used to find a_{EX} and b_{EX}.

B. Resonant Terms

For the resonant contributions to a and b we write a_R and b_R in terms of partial-wave amplitudes $T_L^{\pm}$, each having orbital angular momentum L, parity $(-1)^L$, and spin $J=L\pm\frac{1}{2}$:

$$a_R = \frac{1}{|\vec{k}_1|} \begin{bmatrix} L\ T_L^- \\ \\ (L+1)\ T_L^+ \end{bmatrix} P_L(\cos\theta) \tag{9a}$$

$$b_R = \frac{1}{|\vec{k}_1|} \begin{bmatrix} T_L^- \\ \\ -T_L^+ \end{bmatrix} \frac{dP_L(\cos\theta)}{d\cos\theta} \quad . \qquad (9b)$$

The energy dependence of a_R and b_R are contained in the T_L and the angular dependence, in the Legendre polynomials of the first kind $P_L(\cos\theta)$ and their first derivatives. Table III displays a_R and b_R for various L values along with T_L in spectroscopic and J^P notations. The final state parity P is found from $P=(-1)^L P_M P_B = -(-1)^L$ for a pseudoscalar meson M and even-parity baryon B. The energy dependence of the partial-wave amplitudes is not known in general, but for a resonant state, we approximate the amplitude T_L by the well-known Breit-Wigner form

$$T_L = \tfrac{1}{2} \frac{(\Gamma_i \Gamma_f)^{1/2}}{E_R - w - i\,\tfrac{1}{2}\Gamma} \quad ,$$

where Γ is the full width of the resonance, Γ_i and Γ_f are the partial widths in the entrance (elastic) and final (reaction) channels, and E_R is its energy. The full width Γ is summed over all decay channels of the resonance. There have been several attempts[21] to approximate the energy dependence of the partial widths to take account of angular momentum barrier and phase space effects. The parameterization in this analysis, due to Glashow and Rosenfeld,[22] is

$$\Gamma_k \;\alpha\; \left(\frac{q_k^2}{q_k^2 + X^2} \right)^{L_k} \frac{q_k}{w} \quad ,$$

where q_k and L_k are the c.m. momentum and orbital angular momentum of the kth decay channel products of the resonance, and X is a mass characterizing the radius of interaction. In a fit to partial widths of baryon resonances, Glashow and Rosenfeld[22] found X=350 MeV. When

Table III. Non-spin-flip and spin-flip amplitudes a_R and b_R for various partial waves in their common notations. Here $x=\cos\theta_{cm}$ and $k=|\vec{k}_1|$.

L	$T_L^{\pm}$	L 2J	J^P	a_R	b_R
0	T_0^+	S1	$\frac{1}{2}^-$	$\frac{1}{k}\ T_0^+$	0
1	T_1^-	P1	$\frac{1}{2}^+$	$\frac{1}{k}\ x\ T_1^-$	$\frac{1}{k}\ T_1^-$
1	T_1^+	P3	$\frac{3}{2}^+$	$\frac{1}{k}\ 2x\ T_1^+$	$-\frac{1}{k}\ T_1^+$
2	T_2^-	D3	$\frac{3}{2}^-$	$\frac{1}{k}\ (3x^2 - 1)\ T_2^-$	$\frac{1}{k}\ 3x\ T_2^-$
2	T_2^+	D5	$\frac{5}{2}^-$	$\frac{1}{k}\ \frac{3}{2}\ (3x^2 - 1)\ T_2^+$	$-\frac{1}{k}\ 3x\ T_2^+$
3	T_3^-	F5	$\frac{5}{2}^+$	$\frac{1}{k}\ \frac{3}{2}\ (5x^3 - 3x)\ T_3^-$	$\frac{1}{k}\ \frac{3}{2}\ (5x^2 - 1)\ T_3^-$
3	T_3^+	F7	$\frac{7}{2}^+$	$\frac{1}{k}\ 2\ (5x^3 - 3x)\ T_3^+$	$-\frac{1}{k}\ \frac{3}{2}\ (5x^2 - 1)\ T_3^+$
4	T_4^-	G7	$\frac{7}{2}^-$	$\frac{1}{k}\ \frac{1}{2}\ (35x^4 - 30x^2 + 3)\ T_4^-$	$\frac{1}{k}\ \frac{5}{2}\ (7x^3 - 3x)\ T_4^-$
4	T_4^+	G9	$\frac{9}{2}^-$	$\frac{1}{k}\ \frac{5}{8}\ (35x^4 - 30x^2 + 3)\ T_4^+$	$\frac{1}{k}\ \frac{5}{2}\ (7x^3 - 3x)\ T_4^+$

X is small (large) compared to q_k, the radius of interaction is large (small). Fits to the present data show an improvement for X=175 MeV, but this was too slight to point definitely to a preferred value for X. All results reported herein keep X fixed at 350 MeV. For a single resonant state reaction channel, we may write

$$T_L = \frac{\left[x_i\ (1 - x_i)\right]^{1/2}}{\epsilon - i} \leq \frac{1/2}{\epsilon - i} \quad ,$$

where $x_i = (\Gamma_i/\Gamma) = 1 - x_f$ and $\epsilon = (E_R - w)/1/2\ \Gamma$. This describes a circle centered at (0,i/4) and of diameter 0.5, the unitary limit for resonant partial-wave amplitudes. Fig. 11 shows the complex T plane with the unitary bounds for a resonant state. The circle centered at the origin with radius 0.5 is the limit for partial-wave amplitudes in a reaction channel. There are two possible trajectories for a resonance, depending on the sign of the numerator in T_L. There is in addition an overall phase degeneracy, since I and IP_Λ are unchanged by making the replacement $T_L \rightarrow T_L e^{i\varphi}$. We take this into account by defining the phase of one of the partial-wave amplitudes; all other resonant amplitudes then have phases relative to this fixed phase.

C. Exchange Terms

We assume that the exchange contributions to a and b come from the terms representing K^* -exchange in the t-channel and to nucleon exchange in the u-channel. The contribution due to the Σ pole in the s-channel was considered as well, but the comparison between the theory and data was insensitive to its presence. Pseudoscalar exchange ($J^P=0^-$) such as a pion is forbidden by selection rules at the strong interaction vertices of the diagrams; e.g., conservation of strangeness, angular momentum, parity, and baryon number. The exchange calculations are standard.[20]

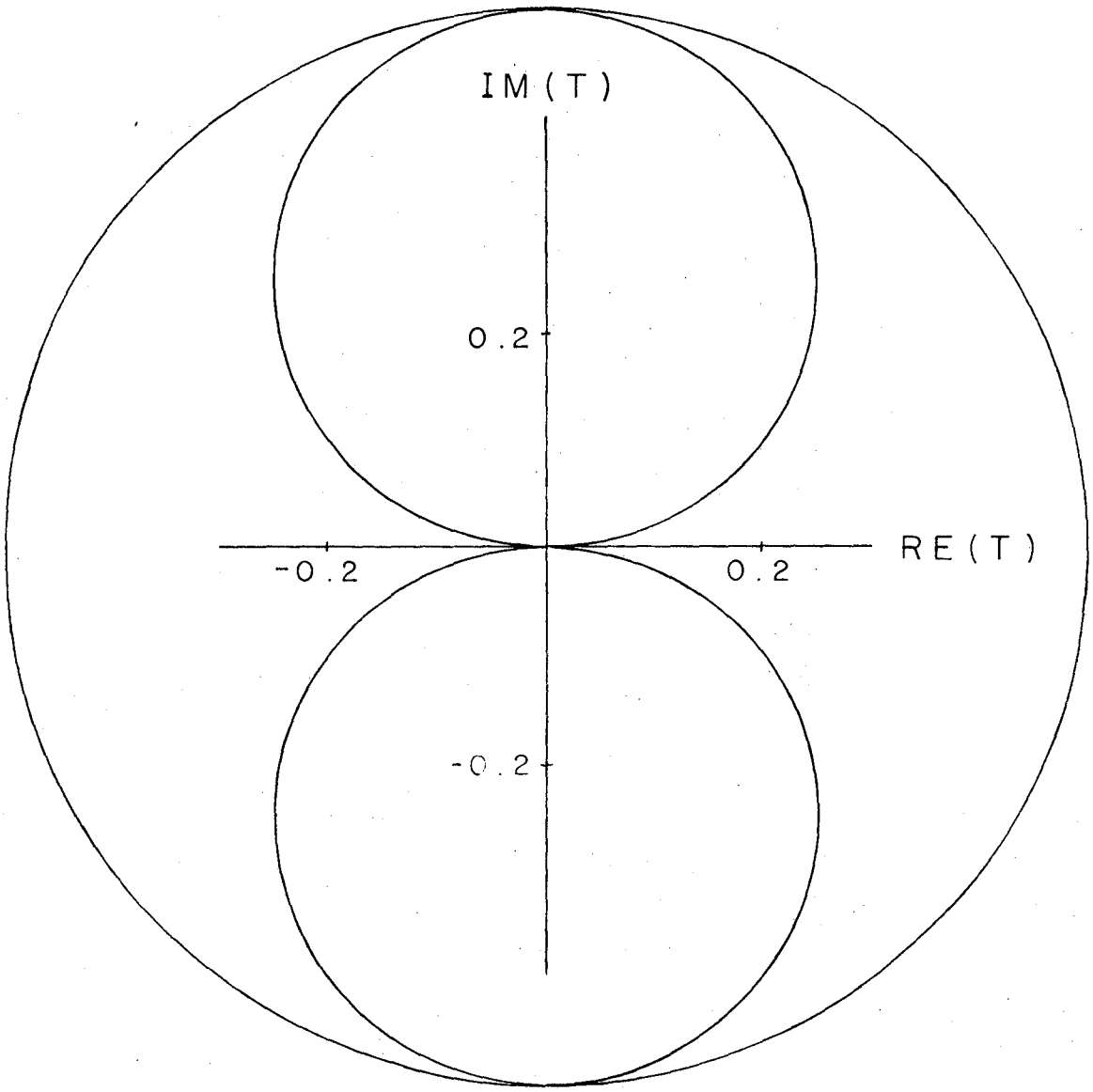

XBL 688-5656

Fig. 11

1. For the exchange of a vector meson K^* with mass M, the invariant amplitude can be constructed from the meson vertex factor

$$g\ (k_1 + k_2)_\mu\ e_\mu \quad ,$$

the baryon vertex factor

$$\bar{u}_\Lambda(p_2) \left[G_V \gamma_\nu + iG_T \frac{\sigma_{\nu\lambda}}{m_1 + m_2} q_\lambda \right] u_p(p_1)\ e_\nu \quad ,$$

and the vector meson propagator

$$\frac{-g_{\mu\nu} + \frac{q_\mu q_\nu}{M^2}}{q^2 - M^2} \quad ,$$

where g is the coupling constant at the meson vertex and G_V (G_T) is the vector (tensor) coupling constant at the baryon vertex. The metric is $g_{\mu\nu}=(1,-1,-1,-1)$, q_μ is the 4-momentum transfer, and e_μ is the unit polarization vector of the K^*. The amplitude can be cast in the form of equation (4) by making the identities

$$A_t = C_t \left[\frac{gG_T}{m_1 + m_2} \left(2w^2 - 2k_{10}k_{20} + 2|\vec{k}_1||\vec{k}_2| \cos\theta - m_1^2 - m_2^2\right) \right.$$

$$\left. - \frac{gG_V}{M^2} \left(\mu_2^2 - \mu_1^2\right) (m_2 - m_1) \right]$$

and

$$\frac{B_t}{2} = -C_t\ (gG_V + gG_T) \ .$$

Here

$$C_t = \frac{1}{2|\vec{k}_1||\vec{k}_2|\ (z_t - \cos\theta)}$$

and

$$z_t = \frac{2k_{10}k_{20} - \mu_2^2 - \mu_1^2 + M^2}{2\,|\vec{k}_1||\vec{k}_2|} \quad .$$

The quantities μ_1 (μ_2) and k_{10} (k_{20}) are the mass and c.m. energy of the initial (final) meson. The contributions a_t and b_t to a and b can now be obtained by means of equations (5) and (6).

2. The invariant amplitude for nucleon exchange in the u-channel is

$$F = g_1 g_2\, \bar{u}_\Lambda(p_2)\, \gamma_5\, \frac{1}{\gamma \cdot Q - m_1}\, \gamma_5\, u_p(p_1) \quad ,$$

where

$$Q = p_2 - k_1 = p_1 - k_2 \quad ,$$

which, when written in the form of (4), yields

$$A_u = \tfrac{1}{2}\, g_1 g_2\, C_u\, (m_2 - m_1)$$

and

$$\frac{B_u}{2} = -\tfrac{1}{2}\, g_1 g_2\, C_u \quad ,$$

where

$$C_u = \frac{1}{2|\vec{k}_1||\vec{k}_2|\,(z_u + \cos\theta)}$$

and

$$z_u = \frac{2k_{10}E_2 - m_2^2 - \mu_1^2 + m_1^2}{2|\vec{k}_1||\vec{k}_2|} \quad .$$

Here g_1 (g_2) is the coupling at the $K\Lambda$ ($N\pi$) vertex. As in the previous case, the contributions a_u and b_u to a and b can be found using equations (5) and (6).

To compare the resonant amplitudes with the exchange terms, we first write the latter in the form (cf. equation (9)):

$$a_{EX} = \frac{1}{k} \sum (L\, T_L^- + (L+1)\, T_L^+)\, P_L(\cos\theta)$$

and

$$\sin\theta\ \ b_{EX} = \frac{1}{k} \sum (T_L^- - T_L^+)\, P_L^1\ (\cos\theta)\ \ ,$$

where $P_L^1\ (\cos\theta)$ is the first associated Legendre function of the first kind, and then project out the exchange partial wave amplitudes in the direct channel by means of relations such as[23]

$$Q_L(z_t) = \frac{1}{2} \int_{-1}^{+1} \frac{P_L(\cos\theta)}{z_t - \cos\theta}\ d\cos\theta$$

and

$$Q_L^1(z_t) = -\frac{1}{2}\ \frac{1}{(z_t^2 - 1)^{1/2}} \int_{-1}^{+1} \frac{\sin\theta}{z_t - \cos\theta}\, P_L^1(\cos\theta)\, d\cos\theta\ ,$$

where $Q_L(z_t)$ is the Lth degree Legendre polynomial of the second kind and $Q_L^1(z_t)$ is thefirst associated Legendre function of the second kind. The Q_L^1 may be expressed in terms of the Q_L, which in turn may be written in terms of logarithms.[24] We can then compare directly the resonant partial-wave amplitudes with the first few exchange partial-wave amplitudes in the complex T-plane.

V. EXPERIMENTAL RESULTS

In this section we discuss the experimental angular distributions, Λ polarizations, and total cross sections.

A. $\Lambda\pi^0$ Cross Sections

During the early stages of the experiment, the topologies scanned for included both 0-prong+V and 2-prong+V events. This latter topology consists of a beam track branching into two visible tracks with an associated V-like decay. Since all of the film was completely rescanned, the numbers of 0- and 2-prong+V events was very accurately determined. These numbers are 2% larger than the numbers of events which successfully passed some hypothesis. This loss of events is attributed to bookkeeping errors, and the 5% error in the cross section for a single event (Table I) includes this factor.

The cross section, σ_{TOT}, for 0- and 2-prong+V events is calculated by multiplying the number, N_{TOT}, of these events, corrected for scanning efficiency, by the cross section for a single event (Table I). The cross section, σ_{0+V}, for 0-prong+V events is then calculated by multiplying σ_{TOT} by the ratio $N_{0+V}/(N_{0+V}+N_{2+V})$, where N_{0+V} and N_{2+V} are the numbers of 0-prong+V and 2-prong+V events found. There is approximately a 1% discrepancy between N_{TOT} and $(N_{0+V}+N_{2+V})$ because of a number of ambiguous events which could not be identified definitely as either topology.

From Sections III D and E, the average weight, $W_{\Lambda\pi}$, can be found at each energy for those events which satisfy the fiducial volume, length, χ^2(1C), and m^2 criteria. The weighted number of $\Lambda\pi^0$ events, $N_{\Lambda\pi}(w)$, may then be calculated from

$$N_{\Lambda\pi}(w) = W_{\Lambda\pi} N_{\Lambda\pi}(u) \quad ,$$

where $N_{\Lambda\pi}(u)$ is the unweighted number of $\Lambda\pi^0$ events. Since the visible decay $\Lambda \rightarrow \pi^- + p$ represents 65.3%[11] of the possible decay modes, the corrected number of $\Lambda\pi^0$ events, $N_{\Lambda\pi}(c)$, is determined by multiplying $N_{\Lambda\pi}(w)$ by 1/0.653.

The $\Lambda\pi^0$ cross section, $\sigma_{\Lambda\pi}$, is then determined by multiplying σ_{0+V}

by the ratio $N_{\Lambda\pi}(c)/N_{0+V}$. See Tables II and IV for a summary. The statistical errors noted range from 4-11%. The $\sigma_{\Lambda\pi}$ cross sections for this experiment are plotted in Fig. 12 along with the data points of Armenteros et al.[25] A report of our $\sigma_{\Lambda\pi}$ has appeared earlier.[26]

B. Angular Distributions

The amounts of film exposed at the various momenta were not constant, as Table I shows, so that the number of $\Lambda\pi^0$ ranges from 113 (unweighted) at the lowest momentum up to about eight-and-one-half times this at the lengthiest exposure (Table II). At each momentum we first divided the events into twenty intervals in the c.m. production cosine. If the number of events in any one interval was less than ten, we combined intervals until this minimum was met. The statistical error for each of the intervals was then calculated as the ratio of the number of weighted events to the square root of the number of unweighted events. The angular distributions are displayed in Fig. 13 and listed in Table V.

C. Λ Polarization

We calculated the Λ polarization P_Λ by first dividing the c.m. production cosine into intervals, each having a minimum of about 40 events. This would produce a maximum error of roughly 0.4 unit, compared to the total P_Λ range of 2 units. The polarization was then determined according to

$$P_\Lambda = \frac{3}{\alpha_\Lambda N_w} \sum_{i=1}^{N_u} W_i x_i ,$$

where W_i is the weight for the ith event and x_i is the cosine of the angle of the decay proton with respect to the production normal $\vec{n}$ defined

Table IV. Cross sections.

Beam momentum	821	878	888	923	946	975	1019	1057	1112
Number of									
0- and 2-prong+V	810	1821	1116	6385	1179	7313	8620	3555	2660
0-prong+V	506	1167	703	4145	795	4699	5431	2233	1623
corrected $\Lambda\pi^0$	276	737	406	2330	419	2274	2078	778	496
Cross sections (mb)									
σ_{TOT}(0- and 2-prong+V)	8.07	8.12	9.00	9.59	10.78	10.27	10.97	11.13	9.95
σ_{0+V}	5.09	5.26	5.69	6.34	7.31	6.69	7.05	7.07	6.16
$\sigma_{\Lambda\pi}$	2.84 ±0.32	3.13 ±0.22	3.42 ±0.31	3.53 ±0.14	3.62 ±0.33	3.19 ±0.12	2.72 ±0.10	2.40 ±0.14	1.89 ±0.14

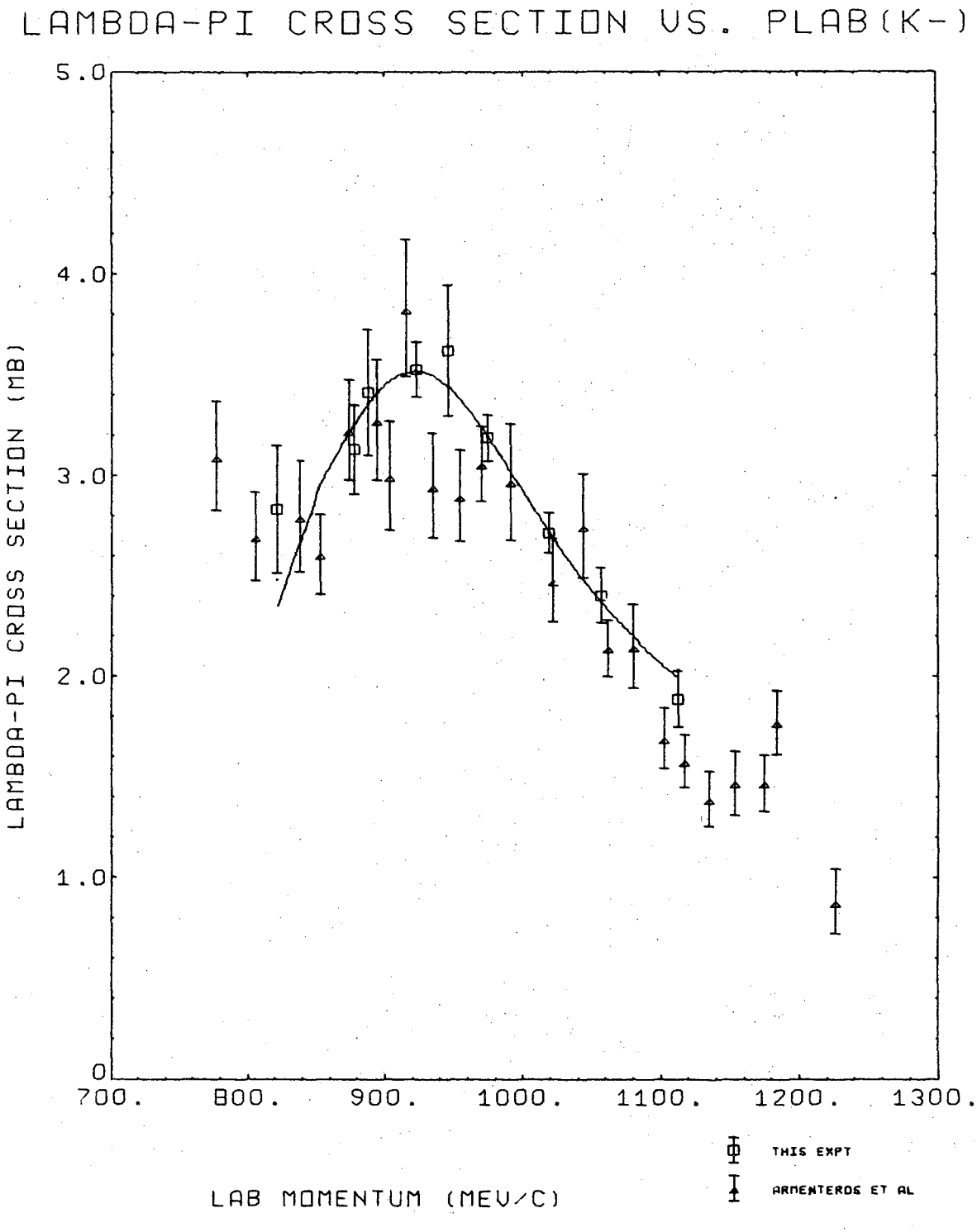

XBL 687-1319

Fig. 12

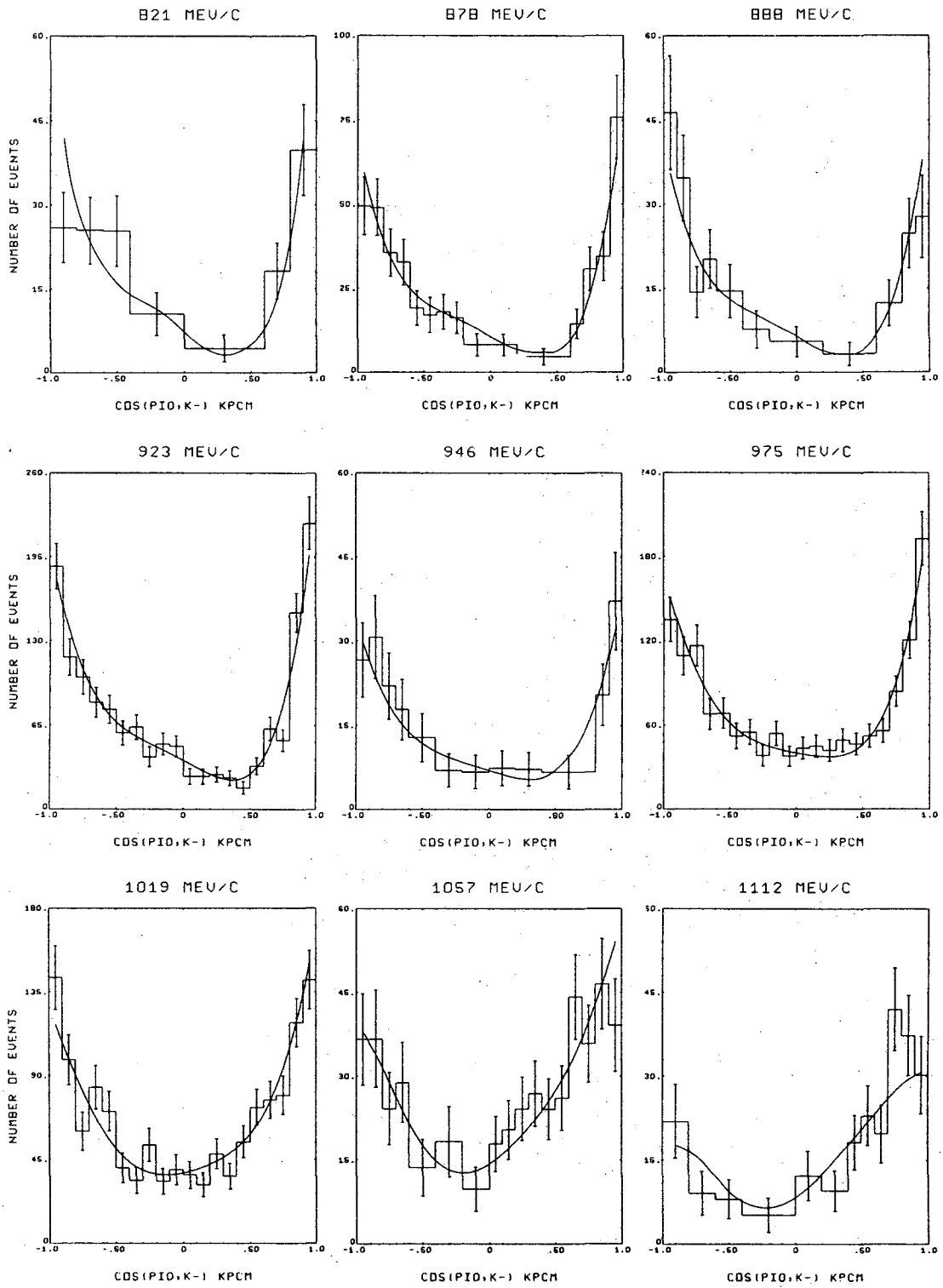

XBL 687-1320

Fig. 13

Table V. Angular distributions for $K^- + p \rightarrow \Lambda + \pi^0$. Asterisks denote the upper limits of the widened intervals in the c.m. production cosines.

cos θ		Momentum (MeV/c) 821	878	888	923	946	975	1019	1057	1112
-1.0	-0.9	25.9±6.3	49.4±8.6	46.3±10.1	187.4±17.6	26.6±6.6	135.0±15.7	142.6±17.2	36.6±8.2	43.7±9.3
-0.9	-0.8	*	49.0±8.5	34.7±7.6	117.3±14.2	30.7±7.4	109.1±13.6	98.5±13.3	36.7±8.7	*
-0.8	-0.7	25.4±6.0	35.5±7.0	14.3±4.5	102.1±13.3	22.0±5.9	116.5±14.5	60.0±10.3	24.2±6.5	18.2±5.5
-0.7	-0.6	*	32.7±6.8	20.2±5.2	82.5±11.7	17.8±5.4	67.8±11.1	83.8±11.7	28.9±7.2	*
-0.6	-0.5	25.3±6.3	19.1±5.1	28.9±6.8	77.2±11.1	25.5±6.0	68.5±10.8	70.9±10.8	27.2±7.0	15.9±5.0
-0.5	-0.4	*	17.1±5.2	*	59.1±9.5	*	52.3±9.2	40.4±7.9	*	*
-0.4	-0.3	21.0±5.4	18.0±5.2	15.4±4.6	63.7±9.6	13.9±4.2	55.0±9.0	33.8±7.0	36.6±8.9	20.9±6.3
-0.3	-0.2	*	16.2±4.7	*	40.7±7.6	*	38.4±7.5	52.8±8.8	*	*
-0.2	-0.1	*	16.4±4.7	22.1±5.4	50.5±8.4	13.4±4.2	54.2±8.7	33.2±6.8	19.6±5.7	*
-0.1	0.0	*	*	*	48.7±8.1	*	38.0±7.1	39.5±8.1	*	*
0.0	0.1	13.3±4.2	16.3±4.5	*	25.5±5.9	14.7±4.4	43.8±7.7	36.7±7.3	17.9±5.0	24.3±6.3
0.1	0.2	*	*	*	25.6±5.9	*	45.2±8.0	31.4±6.4	20.4±5.3	*
0.2	0.3	*	18.9±5.1	13.1±4.1	27.0±6.0	14.3±4.3	42.1±7.7	48.0±8.0	24.2±5.7	18.9±5.1
0.3	0.4	*	*	*	24.4±5.8	*	49.5±8.3	36.1±6.9	26.9±5.9	*
0.4	0.5	*	*	*	16.9±4.9	26.9±6.0	46.7±7.8	54.4±8.5	24.1±5.5	18.2±4.9
0.5	0.6	*	*	*	33.6±6.6	*	52.3±8.3	73.0±9.8	26.1±5.8	22.9±5.4
0.6	0.7	18.2±5.0	14.5±4.4	24.5±5.8	62.5±9.2	*	56.0±8.5	77.1±10.0	44.2±7.6	19.6±5.2
0.7	0.8	*	30.7±6.5	*	53.4±8.6	*	83.9±10.7	79.5±10.4	35.8±6.9	42.0±7.4
0.8	0.9	21.5±5.7	34.4±7.2	24.7±6.2	152.1±15.0	20.4±5.5	120.4±13.2	118.6±13.0	46.5±8.1	37.3±7.2
0.9	1.0	18.3±5.8	75.8±12.3	27.7±7.4	221.0±20.4	37.1±8.7	192.8±19.3	141.4±15.7	39.1±8.3	30.2±6.9

in Section IV A. Our value for the asymmetry parameter is $\alpha_\Lambda = 0.66$[27] and N_u (N_w) is the number of events (weighted events) in each interval. The error in the polarization was calculated from[28]

$$\Delta P_\Lambda = \frac{1}{\alpha_\Lambda} \left(\frac{3 - (\alpha_\Lambda P_\Lambda)^2}{N_w} \right)^{1/2} .$$

The P_Λ distributions are presented in Table VI and displayed in Fig. 14.

Table VI. Lambda polarizations for $K^- + p \rightarrow \Lambda + \pi^0$. Asterisks denote the upper limits of the widened c.m. production cosine intervals.

cos θ		Momentum (MeV/c)								
		821	878	888	923	946	975	1019	1057	1112
-1.0	-0.8	0.67±.034	-0.04±0.25	0.24±0.29	0.19±0.15	-0.21±0.34	0.11±0.16	-0.04±0.16	-0.10±0.30	0.67±.038
-0.8	-0.6	*	-0.41±0.31	-0.29±0.32	0.15±0.19	-0.02±0.32	0.09±0.19	-0.02±0.22	0.34±0.35	-1.06±0.33
-0.6	-0.4	-0.34±0.43	0.25±0.30	*	0.04±0.22	*	-0.16±0.23	-0.02±0.24	0.11±0.31	*
-0.4	-0.2	*	*	0.14±0.36	0.61±0.24	0.26±0.39	0.43±0.27	-0.11±0.28	*	*
-0.2	0.0	-0.41±0.39	-0.54±0.35	*	0.86±0.25	*	0.51±0.26	0.53±0.29	0.40±0.34	0.56±0.35
0.0	0.2	*	*	*	0.73±0.34	*	1.21±0.24	0.77±0.30	*	*
0.2	0.4	*	*	*	0.21±0.36	-0.05±0.40	0.60±0.26	0.94±0.26	1.05±0.33	*
0.4	0.6	*	*	*	-0.62±0.35	*	-0.36±0.25	-0.53±0.22	-0.57±0.35	0.37±0.40
0.6	0.8	*	-0.36±0.38	-0.25±0.29	-0.96±0.22	*	-0.91±0.20	-0.40±0.20	-0.38±0.28	-0.25±0.33
0.8	1.0	-0.20±0.39	-0.42±0.24	*	-0.74±0.13	-0.45±0.34	-0.55±0.14	-0.94±0.15	-0.55±0.27	-0.83±0.29

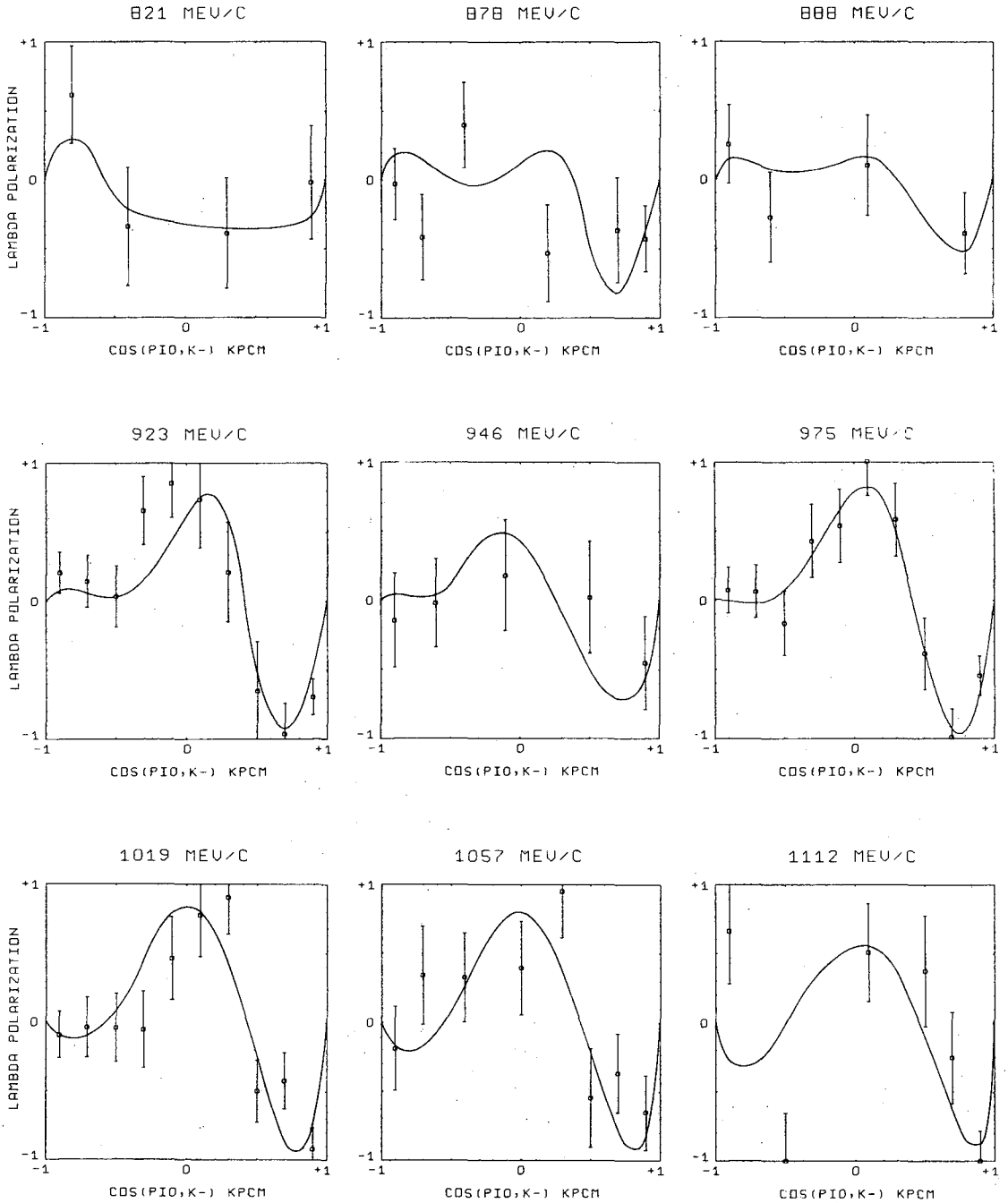

XBL 687-1321

Fig. 14

VI. DISCUSSION OF RESULTS

A χ^2-minimizing program is used to compare the experimental data presented in Section V with the theoretical functions in Section IV. The various solutions reached represent the presence or absence of particular background exchange terms and the resonant amplitudes. The primary aim of this study is to investigate the nature of the background terms in the scattering amplitude required to fit our data. Modifications to the analysis, if the assumptions of the absorption model are introduced, are considered. Other goals of the analysis are to confirm previous spin-parity assignments of the Y_1^* resonances considered, ascertain the relative importance of the terms in the total amplitude, and determine the best-solution parameters.

A. Fitting Procedure

The possible free parameters in this analysis are the amplitude $(x_{\bar{K}N} x_{\Lambda\pi})^{1/2}$, E_R, Γ, and φ for each resonance, and the coupling constant products and arbitrary phases for the exchanges. If these quantities are known, then the resonant and exchange contributions to a and b may be found and the differential cross sections and Λ polarizations (equations (7) and (8)) may be calculated. We first compute the areas under I and IP_Λ for intervals in the production angle cosines corresponding to the experimental angular distributions and Λ polarizations. The theoretical P_Λ's are the average polarizations IP_Λ/I over particular intervals in cos θ. The areas under I and the theoretical P_Λ's are then compared with the experimental data. The number of degrees of freedom, n_D, is n-m-9 for a particular fit, where n is the number of data points, m is the number of parameters allowed to vary, and there are an additional nine fewer degrees of freedom because the calculated angular

distributions (i.e., differential cross sections) are normalized to the number of events at each of the energies.

A reasonable guess for the starting values of the parameters which characterize each hypothesis enables the calculation of the angular distributions, polarizations, and cross sections. A χ^2 was determined by comparing these calculated quantities with the experimental data points and their errors. We used 135 angular distribution points, 63 polarization values, and nine cross sections for a total of 207 data points for the fits. χ^2 was minimized using the program VARMIT,[29] which requires the calculation of the first derivatives of χ^2 with respect to each of the parameters in order to determine the local minimum by means of an iterative variable metric method.[30]

The m-dimensional χ^2-surface undoubtedly has many "valleys", and VARMIT is capable of determining only a local minimum representing a set of parameters closest to the starting values. To face this problem of the uniqueness of a solution, the starting values were changed from a particular set of minimum values, and the minimizing routine was repeated to see if the same solution was reached. Our confidence in the solution is thus increased, but there always remains the possibility of other solutions.

The fits of the various hypotheses to the experimental data can be compared by examining the lowest χ^2 reached in each case, and in calculating the confidence level, given by

$$\text{C.L.} \approx \frac{1}{\sqrt{2\pi}} \int_y^\infty \exp(-\tfrac{1}{2} x^2)\, dx \quad ,$$

where

$$y = \sqrt{2\chi^2} - \sqrt{2n_D - 1} \quad .$$

This is the probability that a χ^2 larger than the experimental value would have been obtained, or alternatively, that another experiment would give a poorer fit. The equation is approximately valid for $n_D > 30$.

B. Selected Solutions

The resonant energy of the $Y_1^*(1770)$ is well-centered in our c.m. energy region from 1700 to 1850 MeV. Other Y_1^* resonances outside this range but which may affect the angular distributions and polarizations to some degree are (masses and widths from reference 11):

1. $Y_1^*(1660)$, Γ=50 MeV. This resonance is consistent with $J^P=3/2^-$. Published values of the branching ratios $x_{\bar{K}N}$ and $x_{\Lambda\pi}$ conflict with each other. However, $x_{\bar{K}N}x_{\Lambda\pi} \approx 0.01$.[4,31]

2. $Y_1^*(1690)$, Γ=120 MeV. The J^P for this enhancement is not known, and we have not attempted to probe this Y_1^*.

3. $Y_1^*(1910)$, Γ=60 MeV. This effect, still not completely established, has $J^P=5/2^+$, $x_{\bar{K}N} \approx 0.1$,[32,33] and $x_{\bar{K}N}x_{\Lambda\pi} \approx 0.01$.[4,27]

4. $Y_1^*(2030)$, Γ=120 MeV. For this resonance, $J^P=7/2^+$, $x_{\bar{K}N}=0.25$, and $x_{\Lambda\pi}=0.16$.[34] The partial-wave analysis of Smart et al.[4] gives $x_{\bar{K}N}x_{\Lambda\pi}=0.14$.

In performing the analysis, we start out with fairly simple assumptions and then gradually increase the number of amplitudes contributing to the reaction $K^- + p \rightarrow \Lambda + \pi^0$. We allow $(x_{\bar{K}N}x_{\Lambda\pi})^{1/2}$, E_R, and Γ of the $Y_1^*(1770)$ to vary, but only permit the amplitudes and the relative phases of the other resonant terms to change. As a convention, we fix $\varphi=0°$ for $Y_1^*(1770)$. The background parameters are discussed more explicitly later.

Initially, we sought a solution using a D5 resonant amplitude, representing $Y_1^*(1770)$, along with real t- and u-channel exchange terms; for a second trial, D5 was replaced by an F5 resonant amplitude. Although

neither hypothesis was adequate to fit the data, as is obvious from the C.L.'s for solution 1 in Table VII A, the relative confidence level is

$$R(D5/F5) \equiv \frac{C.L.(D5)}{C.L.(F5)} = 10^{42} .$$

The data clearly prefer D5, and in subsequent cases we assume $Y_1^*(1770)$ is present and characterize it as $J^P=5/2^-$ (D5).

As confirmation of the parity of $Y_1^*(2030)$, solutions 2-5 were constructed to test both $J^P=7/2^+$ and $7/2^-$ (F7 and G7) possibilities. Real background exchanges were used by fixing the phases of these terms at 0° and 180°. Resonant F5 and D3 amplitudes, representing $Y_1^*(1910)$ and $Y_1^*(1660)$, were added one at a time. The relative C.L.'s for these solutions favor F7 over G7 in every case, with $R(F7/G7)=10^7$, 10^8, 10^5, and 10^2. Hence $J^P=7/2^+$ is confirmed for $Y_1^*(2030)$, in agreement with the original analysis of Wohl et al.[34]

We next tested the parity of $Y_1^*(1660)$ as $J^P=3/2^-$ and $3/2^+$ (D3 and P3) in solutions 5-7 with real background terms and resonant F5 and F7 amplitudes present. The relative C.L.'s are R(D3/P3)=10, 10, and 6. Although the discrimination is weaker than for the previous trials, in each case D3 is favored over P3. Thus $J^P=3/2^-$ is confirmed for $Y_1^*(1660)$, in agreement with the assignment originally proposed by Alvarez et al.[31]

The resonant partial waves and the partial-wave projections of the exchange terms are plotted in Fig. 15A for solution 5a. Even for this solution, the best so far, the probability of fit is still very low (C.L.$\approx 10^{-8}$). The S1-, P1-, and P3-wave contributions arise solely from the exchange terms, which are real; we fixed $\varphi=0°(180°)$ for the t- (u-) channel exchange term. To keep these lower partial waves real is to say that no other processes are taking place; the low probability of fit

Table VII. Amplitudes and terms used to fit the experimental angular distributions, Λ polarizations, and $\Lambda\pi^0$ cross sections. The number of degrees of freedom is given by n_D=n-m-9, where n=207 data points and m=number of free parameters.

A. Solutions for real background exchange terms.

Fit	Resonant amplitudes	Exchange terms	χ^2	m	n_D	C.L.
1a	D5	t u	418	6	192	10^{-21}
b	F5	t u	662	6	192	10^{-63}
2a	D5 F7	t	370	7	191	10^{-14}
b	D5 G7	t	422	7	191	10^{-21}
3a	D5 F7	t u	359	8	190	10^{-13}
b	D5 G7	t u	417	8	190	2×10^{-21}
4a	D5 F5 F7	t u	338	10	188	3×10^{-11}
b	D5 F5 G7	t u	377	10	188	3×10^{-16}
5a	D5 F5 F7 D3	t u	315	12	186	5×10^{-9}
b	D5 F5 D3 G7	t u	329	12	186	10^{-11}
c	D5 F5 F7 P3	t u	322	12	186	8×10^{-10}
6a	D5 F7 D3	t	339	9	189	3×10^{-11}
b	D5 F7 P3	t	344	9	189	3×10^{-12}
7a	D5 F7 D3	t u	331	10	188	10^{-10}
b	D5 F7 P3	t u	340	10	188	10^{-11}
8	D5 F5 F7 D3	t	321	11	187	2×10^{-9}

Table VII. (continued)

B. Solutions for background exchange terms multiplied by phenomenological factors $e^{i\varphi}$.

Fit	Resonant amplitudes	Exchange terms	χ^2	m	n_D	C.L.
9	D5 F7	t	266	8	190	10^{-4}
10	D5 D3	t	271	8	190	6×10^{-5}
11	D5 F5 F7	t	248	10	188	0.002
12	D5 F5 D3	t	264	10	188	10^{-4}
13	D5 F7 D3	t	244	10	188	0.003
14	D5 F5 F7 D3	t	229	12	186	0.018
15	D5 F7 D3	t u	227	12	186	0.022
16	D5 F5 F7 D3	t u	219	14	184	0.038
17	F5 F7 D3	t u	564	12	186	10^{-46}
18	D5 F5 F7 D3 P1	t u	217	16	182	0.035

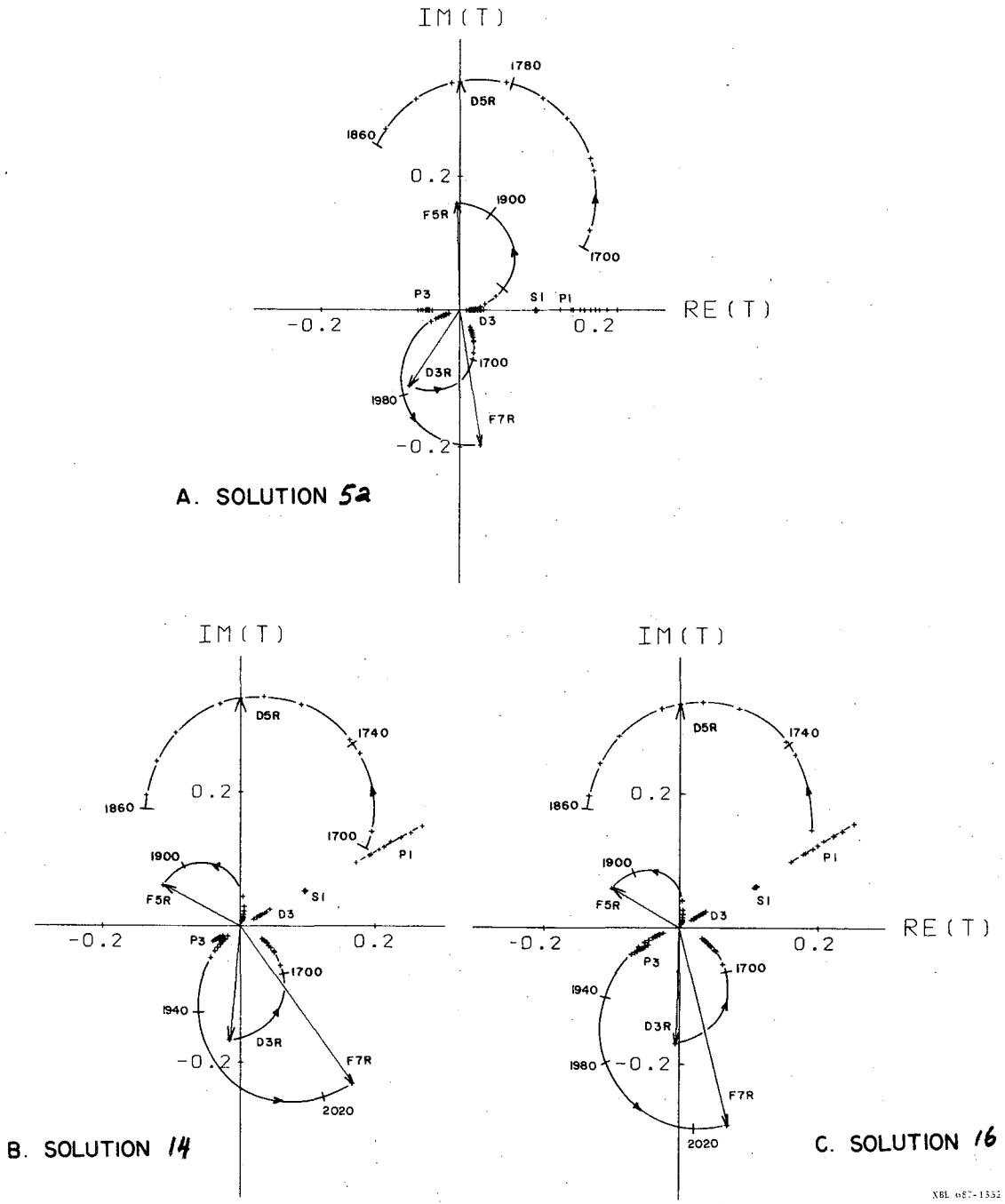

Fig. 15

The amplitudes shown come from the fits to the data for the reaction $K^- + p \rightarrow \Lambda + \pi^0$. The full I=1, $\bar{K}N \rightarrow \Lambda\pi$ amplitudes may be obtained from these by multiplying them by $\sqrt{2}$.

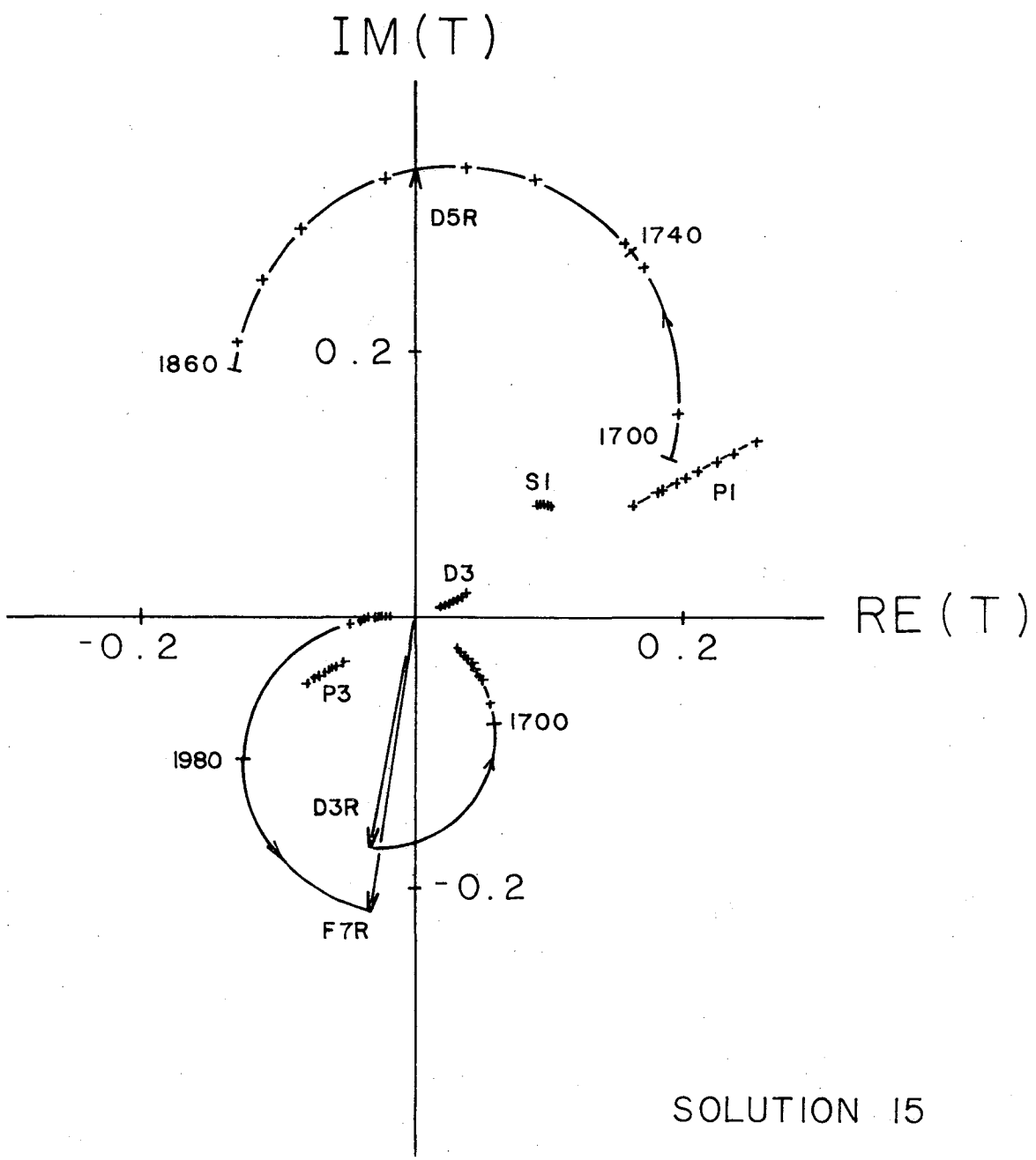

XBL 688-5657

Fig. 16

The amplitudes shown come from the fits to the data for the reaction $K^- + p \rightarrow \Lambda + \pi^0$. The full I=1, $\bar{K}N \rightarrow \Lambda\pi$ amplitudes may be obtained from these by multiplying them by $\sqrt{2}$.

implies that simple exchanges are insufficient to describe the background. To ease this restriction, we may simply multiply one or both exchange terms by phenomenological factors, $e^{i\varphi}$. We have done this, and Table VII B displays the results. A comparison of like resonant and exchange term contributions between the solutions in Tables VII A and B shows a vast improvement in the fits, with relative confidence levels between 10^7 and 10^{10}.

A study of solutions 9-16 in Table VII B reveals the relative importance of the Y_1^* resonances outside our energy range. Relative confidence levels for solutions with and without the F7, D3, and F5 amplitudes are approximately 100, 20, and 10, respectively. The addition of any of these resonances improves the probability of fit, but we can conclude that the F7 is the most important Y_1^*, other than $Y_1^*(1770)$, affecting the angular distributions and polarizations in our energy region. The addition of the u-channel contribution increases C.L. between 2 to 7 times.

Finally, solution 17 demonstrates that the data really prefer D5 over F5, as the assignment for $Y_1^*(1770)$, since C.L.(F5)=10^{-46} and C.L.(D5)=0.022 for solution 15. This gives us added confidence that $Y_1^*(1770)$ indeed has $J^P=5/2^-$.

There has recently[35] been some indication for the existence of a $J^P=1/2^+$ Y_1^* resonance with $(E_R,\Gamma)=(1882,222)$ MeV. We added a P1 resonant amplitude to solution 16, fixing E_R and Γ at the suggested values, and found a solution with C.L.=0.035. Since the fit is only slightly better without the assumption of this term, we conclude that if it is present, its signal is not strong enough to be distinguished in our data.

The three best solutions in this second series of fits have confidence levels in the range 2-4%; solutions 14 and 16 are plotted

in Figs. 15B and C, and solution 15 is shown in Fig. 16. We expect the resonant amplitude, T, to be purely imaginary at the resonant energy $w=E_R$; i.e., the resonant phase angle φ should be 0° or 180° relative to $\varphi=0°$ for D5. From these plots and Table VIII, we see that when the F5 amplitude, $Y_1^*(1910)$, is absent, the relative phases for both F7 and D3 are 180° within errors (solution 15). The inclusion of F5, while slightly improving the probability of fit, yields solutions for which the relative phase requirement is violated by either or both F5 and F7. The conclusion is that the F5 resonant amplitude is not necessary for our data. We do, however, require the u-channel exchange contribution to the background.

C. Comparison With Other Analyses

Table VIII also shows the other resonant parameters which were allowed to vary; they are consistent within errors for these three best solutions. In the last column are the resonant parameter averages for the solutions. The errors presented in this column are simply the average of the errors for the three solutions. The experimental data for the hypotheses are exactly the same, and the errors would be underestimated if the three solutions were to be regarded as independent determinations of the parameters.

The $Y_1^*(1770)$ mass of 1776±4 MeV is consistent with the current average.[11] The width of 152±9 MeV is quite a bit higher, but entirely consistent with the analyses of Smart et al.[4] and of Davies et al.[33] The branching ratio product $x_{\bar{K}N}x_{\Lambda\pi}$ for D5 of 0.222±0.011 is twice that of references 4 and 27; if $Y_1^*(1910)$ is present, $x_{\bar{K}N}x_{\Lambda\pi}=0.028\pm0.018$, consistent with these references. For $Y_1^*(2030)$, we find $x_{\bar{K}N}x_{\Lambda\pi}=0.143\pm0.069$. This value agrees well with that of Smart et al.[4] but is higher than that found by Wohl et al.[34] Finally, for $Y_1^*(1660)$, $x_{\bar{K}N}x_{\Lambda\pi}=0.058\pm0.023$. While the published branching ratios

Table VIII. Resonant parameters from three of the best solutions.

	Solution 14	Solution 15	Solution 16	Average
Resonant amplitude		Relative phase		
D3	175° ± 14°	170° ± 12	179° ± 15°	
D5	0	0	0	
F5	61° ± 29°	---	60° ± 24°	
F7	216° ± 15°	172° ± 9°	193° ± 16°	
		$x_{\bar{K}N}x_{\Lambda\pi}$		
D3	0.057 ± 0.024	0.059 ± 0.022	0.058 ± 0.024	0.058 ± 0.023
D5	0.228 ± 0.011	0.221 ± 0.011	0.218 ± 0.013	0.222 ± 0.011
F5	0.032 ± 0.017	0	0.025 ± 0.018	0.028 ± 0.018
F7	0.162 ± 0.060	0.092 ± 0.058	0.176 ± 0.090	0.143 ± 0.069
		Resonant energy		
D5	1776 ± 4	1777 ± 5	1776 ± 5	1776 ± 4
		Resonant width		
D5	145 ± 8	158 ± 10	152 ± 9	152 ± 9

The masses and widths (E_R,Γ) of $Y_1^*(1660)$, $Y_1^*(1910)$, and $Y_1^*(2030)$ were kept fixed at (1660,50), (1910,60), and (2030,120), respectively. The branching ratio products shown, $x_{\bar{K}N}x_{\Lambda\pi}$, are related to those from the fits, $(x_{K^-p}x_{\Lambda\pi})^{1/2}$, by $x_{\bar{K}N}x_{\Lambda\pi}=2\left[(x_{K^-p}x_{\Lambda\pi})^{1/2}\right]^2$.

$x_{\bar{K}N}$ and $x_{\Lambda\pi}$ show inconsistencies, as noted in Section B above, our value for the branching ratio product agrees with that of London et al.[31] and is somewhat higher than that of Alvarez et al.[31]

Solutions 15 and 16 show that, within errors, the resonant amplitude $Y_1^*(1770)$ is 180° out of phase with $Y_1^*(2030)$ and with $Y_1^*(1660)$ at resonance, in agreement with the findings of Smart et al.[4] The solution 16 phase of 60°±24° for $Y_1^*(1910)$ relative to $Y_1^*(1770)$ is two-and-one-half standard deviations away from 0°; reference 4 found that $Y_1^*(1770)$ was in phase with $Y_1^*(1910)$ at resonance. As noted earlier, our data seem not to be particularly sensitive to the presence of $Y_1^*(1910)$.

As indicated in the Introduction, Smart[4] studied the reaction $K^- + n \rightarrow \Lambda + \pi^-$ in the c.m. energy region 1660-1900 MeV, assuming Y_1^* resonances in the direct channel and four complex background amplitudes which were either constant or mildly energy-dependent. It is significant that the projections of the first few partial-waves of the exchange-channel terms in our model agree with the general orientation and magnitude of the background partial waves of this reference. The implication is that the actual background amplitudes in the complex T-plane for the general reaction $\bar{K}N \rightarrow \Lambda\pi$ are independent of any particular parameterization. As a final point of comparison, Smart used 15 parameters to achieve C.L.=1.7% when his background terms were constant; when these terms were energy-dependent, C.L.=8.3% for 23 parameters. In our model, solution 15, for example, uses 12 parameters and C.L.=2.2%. The numbers of data points in both analyses are comparable.

D. Background Amplitudes

The partial-wave projections of the exchange-channel amplitudes are

consistent among the solutions in Table VII B as to orientation and energy dependence. Moreover, the t-channel exchange parameters for solutions 14-16 are the same within errors, and the u-channel exchange parameters for solutions 15 and 16 also agree. (No u-channel exchange was allowed for solution 14). This indicates a lack of sensitivity of the t-channel parameters as to (1) the presence of F5 and absence of u-channel exchange; (2) the absence of F5 and presence of u-channel exchange; and (3) the presence of both. This is not surprising, since the primary contribution to the reaction is $Y_1^*(1770)$ and all other contributions are small compared to it. We now proceed to a discussion of the exchange-channel parameters within the context of Table IX.

From the full width of the K^* of Γ=49.2 MeV,[11] we can estimate the coupling constant at the $K^*K\pi$ vertex from

$$\frac{1}{3}\Gamma = \frac{2}{3}\,\frac{g^2}{4\pi}\,\frac{p^3}{M^2} \quad ,$$

where p is the momentum of the decay products in the K^* c.m., M is the K^* mass, and the 1/3 comes from the partial width of $K^{*+} \rightarrow K^+ + \pi^0$ being one-third of the total K^* width Γ. Then $g^2/4\pi$=0.81. The average of the absolute values of gG_V and gG_T, from solutions 14-16, are 4.42±0.83 and 30.70±3.36, respectively; these errors are the average of the errors for the solutions, for the reason given in Section C. Using the above value for $g^2/4\pi$, we find from our analysis,

$$\frac{G_V^2}{4\pi} = 0.15 \pm 0.04 \quad ,$$

$$\frac{G_T^2}{4\pi} = 7.34 \pm 1.14 \quad ,$$

Table IX. Exchange channel parameters.

Parameter	Solution 14	Solution 15	Solution 16
gG_V	-6.37 ± 0.67	-2.85 ± 0.73	-4.05 ± 1.09
gG_T	-29.56 ± 3.08	-31.19 ± 3.42	-31.34 ± 3.57
φ_t	29°± 5°	27° ± 5°	31° ± 9°
g_1g_2	0	8.64 ± 1.43	6.29 ± 2.51
φ_u	---	221° ± 10°	208° ± 16°

and

$$\frac{G_T}{G_V} = 6.94 \pm 2.14 \quad .$$

Hoff,[14] in the study of $\pi^- + p \rightarrow \Lambda + K^0$ with the assumption of K^* -exchange, two direct-channel resonances, and no tensor coupling term, finds the product of the square of coupling constants $(gG_V/4\pi)^2=0.155$. If we use the above value for $g^2/4\pi$, then Hoff would find $G_V{}^2/4\pi=0.19$. Our value is consistent with this.

The vector coupling constant for the K^* $N\Lambda$ vertex can be related to that for ρNN by SU(3):[36]

$$\left(\frac{G_V{}^2}{4\pi}\right)_{K^* N\Lambda} = \frac{1}{3}(1 + 2f)^2 \left(\frac{G_V{}^2}{4\pi}\right)_{\rho NN} ,$$

where f=F/F+D = 1/1+R is the symmetric-antisymmetric octet mixing parameter, and R is the D/F ratio. From a study of nucleon-nucleon forces, Scotti and Wong[37] estimate $(G_V{}^2/4\pi)_{\rho NN}=1.27$. If the vector coupling of the vector-meson octet to the baryon octet is of the pure F type,[38] R=0 and f=1, and $(G_V{}^2/4\pi)_{K^*N\Lambda}=3.8$. Our value is about one order of magnitude less. A lower value implies a higher D/F ratio, but even for pure D coupling, with f=0, one would find $(G_V{}^2/4\pi)_{K^*N\Lambda}=0.4$, still somewhat above our determination.

For the tensor coupling constant, a similar form holds:

$$\left(\frac{G_T{}^2}{4\pi}\right)_{K^* N\Lambda} = \frac{1}{3}(1 + 2f)^2 \left(\frac{G_T{}^2}{4\pi}\right)_{\rho NN} .$$

The Scotti and Wong[37] estimate $(G_T{}^2/4\pi)_{\rho NN}=11.4$ implies a range for f

from about zero up to f=0.28. This is within the range $0.15 < f < 0.56$ suggested by Martin and Wali[39] on the basis of a model using single-baryon exchange. Moreover, if the tensor coupling of the vector-meson octet to the baryon octet is primarily of the D type, with the Sakurai[40] value R=3.5, then $(G_T^2/4\pi)_{K^*N\Lambda}=7.9$, consistent with our value.

From studying the electromagnetic baryonic structure,[41] one has the estimate $(G_T/G_V)_{\rho NN}=3.7$. Using

$$\left(\frac{G_T}{G_V}\right)_{K^*N\Lambda} = \frac{1+2f_T}{1+2f_V}\left(\frac{G_T}{G_V}\right)_{\rho NN}$$

and $R_T=3.5$ as before, we find a region $-0.23 < f < 0.18$, suggesting a range from $D/F \approx 5$ up to a pure D type vector coupling of the vector-meson octet to the baryon octet. If one were to assume a pure F type vector coupling, then $(G_T/G_V)_{K^*N\Lambda} \approx 2$. Our higher G_T/G_V ratio implies (1) a smaller D/F ratio for the tensor coupling, (2) a larger D/F ratio for the vector coupling, or (3) both. For example, if $R_T=0$ and $R_V=3/2$, then $G_T/G_V \approx 6.2$.

For the u-channel exchange, the pertinent vertices are $KN\Lambda$ and πNN. The πNN coupling constant is fairly well-known, $g_2^2/4\pi=15$. Then from our analysis, for the $KN\Lambda$ vertex,

$$\frac{g_1^2}{4\pi} = 0.024 \pm 0.009 \quad .$$

Warnock and Frye,[42] in a study of low-energy KN scattering, find two best fits to the data, both consistent with $g_1^2/4\pi=0$. Our value is also consistent with zero. On the other hand, from SU(3) invariance,

$$\frac{g_1^2}{4\pi} = \frac{1}{3}(1 + 2f)^2 \frac{g_2^2}{4\pi} \quad .$$

The above Martin and Wali[39] range for f implies $8.5 < g_1^2/4\pi < 22.5$, and using modified dispersion relations, Chan and Meiere[42] predict $g_1^2/4\pi = 13 \pm 3$, compatible with SU(3) invariance. Our value is at least two orders of magnitude below these predictions.

To summarize, the background parameter values from our analysis, $G_V^2/4\pi$ for the $K^*N\Lambda$ vertex and $g_1^2/4\pi$ for the $KN\Lambda$ vertex, are consistent with other experimental fits but low compared to theoretical predictions. Both $G_T^2/4\pi$ and G_T/G_V for the $K^*N\Lambda$ vertex agree with theoretical predictions.

We also take note here of the various contributions to the angular distributions. The resonant contribution is due primarily to $Y_1^*(1770)$ (D5). The interference between the resonant states and the t-channel is mainly a D5-P1 partial-wave interaction, giving rise to constructive (destructive) interference in the forward (backward) direction. The resonant-u-channel interference comes from principally D5 and S1 partial waves interacting, producing constructive interference in both forward and backward directions. The small t-channel and u-channel interference arises from an S1-P1 term, giving constructive (destructive) interference in the forward (backward) direction. It should be noted that the resonant term comprises 70-80% of the total amplitude. Table X shows the qualitative contributions of the various terms to regions of the angular distributions and Λ polarizations. The background exchange terms, although small in themselves, interfere with the primary (resonant) interaction to produce more pronounced peaking in both forward and backward directions in the angular distributions.

Table X. Qualitative contributions of various terms to regions of the angular distributions and Λ polarizations. R, t, and u denote resonant, t-channel, and u-channel contributions.

	A. Angular distributions		B. Λ polarizations		
Term	Backward	Forward	Backward	Central	Forward
R	+	+	0	-	-
t	0	+	0	0	0
u	+	0	0	0	0
R-t	-	+	-	+	-
R-u	+	+	+	0	-
t-u	-	+	0	-	0

E. Absorption Considerations

As we have seen, the inclusion of phenomenological factors $e^{i\varphi}$ for the exchange terms to try to account for other processes which may be taking place improves the probability of fit by seven-ten orders of magnitude. If, instead, we were to take absorption into account, we would conventionally multiply the projected partial-wave amplitudes by the factors[44]

$$\left[1 - C_+ e^{-\gamma_+(x-\frac{1}{2})^2}\right]^{\frac{1}{2}} \left[1 - C_- e^{-\gamma_-(x-\frac{1}{2})^2}\right]^{\frac{1}{2}} ,$$

where the variable x is the total angular momentum, $J_0 \leq x < \infty$. When $C \pm = 1$, this form represents complete absorption for the lowest partial wave contributing to amplitudes with $J_0 = \frac{1}{2}$. The initial (+) channel parameters may be taken from elastic scattering data,

$$C_+ = \frac{\sigma_{TOT}}{4\pi A}$$

and

$$\gamma_+ = \frac{1}{2k^2 A} ,$$

where σ_{TOT} is the total cross section, k is the incident c.m. momentum, and A is the elastic-scattering slope parameter, obtained from

$$\frac{d\sigma}{dt} = \frac{\pi}{k^2} \frac{d\sigma}{d\Omega} \propto e^{At}$$

for the elastic-scattering differential cross section. From the elastic $K^- p$ data of Gelfand et al.[45] and the total cross section data of Bugg et al.[46] we estimate $C_+ \approx 0.4$ and $\gamma_+ \approx 0.2$ near 975 MeV/c. (This may be compared with $(C_+, \gamma_+) = (0.64, 0.05)$ at 3 BeV/c,[44]) Since $\Lambda\pi$ scattering data is not available, we consider instead $(C, \gamma) = (0.765, 0.038)$ for $\pi^- p$ scattering

at 4 BeV/c;[47] scaled to our final-state c.m. momentum of 530 MeV/c, we very roughly estimate our final-state parameters $(C_-,\gamma_-) \approx (0.8,0.2)$. A comparison with the initial-state absorption parameters shows that this choice of (C_-,γ_-) implies a much stronger absorption of the lowest partial waves in the final state.

With these admittedly crude estimates, we find that both S1 and P1 partial waves would be 65% absorbed, P3 and D3 would be 52% absorbed, and D5 would be 27% absorbed. The exchange-channel partial-wave projections are primarily S1, P1, P3, and D3, with P1 the largest. The magnitudes of S1, P3, and D3 relative to P1 are about 50%, 30%, and 15%, respectively; the D5 partial wave is 2% of P1 and all higher partial-wave projections are less than this. If the lowest partial waves were absorbed to some degree, then the coupling constant products would be expected to increase to compensate, and $g_1^2/4\pi$, for example, would be more in line with theoretical predictions. We would also anticipate the t-channel contributing somewhat more forward peaking to the angular distribution if its higher partial waves became more important. However, the t-channel contributes only about 15% to the total $\Lambda\pi^0$ cross sections, so the effect should not be too pronounced. The u-channel contributes even less, about 5%.

The calculated angular distributions already fit well with the experimental data without these assumptions of the absorption model. However, we would expect the fit to the polarization data to be better with the higher background partial waves making relatively larger contributions to our reaction. Hence we would expect absorption to somewhat improve our overall fit, and this process would not be so artificial a method of taking account of other processes taking place.

At higher energies, as more competing channels become open,

undoubtedly absorption would play a more important role. One would expect these more complex reactions to be the result of collisions at small impact parameters; the existence of these other possible final states would reduce the lower partial-wave amplitudes for our own single reaction of interest. A problem common to both unmodified and modified (through absorption) exchange mechanisms, however, is the well-known high-energy violation of unitarity, whether or not one assumes any structure for the vertices; i.e., dependence of the coupling "constants" on momentum transfer. An amplitude involving a t-channel state of angular momentum J is proportional to s^J, where s is the square of the total c.m. energy. Hence for our vector meson K^* -exchange, there will eventually be a violation of unitarity. In our energy range, there is no violation, but one can see that the amplitudes do show an increase with energy. Presumably, at high energies, an alternate description--for example, Regge poles--of the t-channel may be drawn to alleviate this problem.

We now comment here briefly on the possibility of Regge-pole exchange. There is some question about the use of this mechanism in our case, in the first place, since our energies are rather low; in addition, a model which uses both resonances in the direct channel and Regge-pole exchange involves "double-counting", since it has been shown[48] that projecting the Regge amplitude into the direct channel produces circles on the Argand plot corresponding to experimental resonances. More recently, however, it has been argued[49] that these Argand plot circles should not necessarily be interpreted as resonances. This problem is in a momentary state of flux, and we conclude by pointing out that our parameterization of the exchange amplitudes is such that partial-wave projections of these terms cannot form circles on the Argand plot.

VII. SUMMARY

The reaction $K^- + p \rightarrow \Lambda + \pi^0$ has been analyzed with the assumption of direct channel resonances and background exchange amplitudes. Simultaneous fits to the experimental angular distributions, Λ polarizations, and $\Lambda\pi^0$ cross sections have been made over the c.m. energy range 1700-1850 MeV.

Our data have shown strong enough discrimination to confirm the previous J^P assignments of 3/2 - for $Y_1^*(1660)$, 5/2 - for $Y_1^*(1770)$, and 7/2 + for $Y_1^*(2030)$. Our determinations of the branching ratio products $x_{\bar{K}N} x_{\Lambda\pi}$ for $Y_1^*(1660)$ and $Y_1^*(2030)$ are 0.058±0.023 and 0.143±0.069 respectively. Our data are not particularly sensitive to the presence of $Y_1^*(1910)$. To the degree that we can distinguish it, we obtain a value $x_{\bar{K}N} x_{\Lambda\pi}$=0.028±0.018 The $Y_1^*(1770)$ mass, width, and $x_{\bar{K}N} x_{\Lambda\pi}$ are determined to be 1776±4 MeV, 152±9 MeV, and 0.223±0.011, respectively.

Only with additional $e^{i\varphi}$ factors applied to the exchange terms can reasonable fits to the data be achieved. We obtained values of the coupling constant products for both K^* - and nucleon-exchange, but since we ignore structure in the vertices, they should not be taken too seriously, although there is some agreement with the work of others. Taking account of absorption due to competing channels would be a more realistic approach, and should increase the values of our coupling constants.

Finally, we have shown that the assumption of direct channel resonances and a simple parameterization for the background will produce reasonable fits to our experimental data.

ACKNOWLEDGMENTS

I would like to express my appreciation to Professor Robert P. Ely, Jr., for his guidance and instruction throughout most of my graduate studies, and for a critical reading of this paper. Much of the earlier work of this experiment was performed in collaboration with Jack Sahouria, and I have benefited from many fruitful discussions with him. I also thank Nathan Jew for clearing up many questions on theory. The many scanners and measurers under the able supervision of Wes Weber gave fine support; in particular, I would like to thank Mrs. Lois Tinay and Jim Corey for their diligence. Miss Charlotte Scales was of great help in the bookkeeping. I have benefited in many other ways from my association with all members of the Powell-Birge Physics Group.

The services of the Bevatron operations group, bubble chamber crew, film lab technicians, graphic arts personnel, and computer staff were vital to the completion of this experiment. The availability of the CDC 6600 speeded up the computational work considerably.

The work of the Data Handling group, under the direction of Howard White, was indispensible; thanks are due Loren Shalz for help in using the FAIR system.

I thank Derik Armstrong for assistance in using CHAOS to quickly extract information from data tapes, and Mrs. Bronwyn Hall for making her extremely useful plotting programs available. I also acknowledge a useful conversation with Dr. C. Schmid concerning "double-counting".

Mrs. Sandra Paciotti did a fine, conscientious job in typing this paper.

I am grateful to my wife, Emma, for her encouragement and for essential help in the preparation of the drawings.

This work was carried out under the auspices of the U.S. Atomic Energy Commission.

REFERENCES AND FOOTNOTES

1. V. Cook, B. Cork, T. F. Hoang, D. Keefe, L. T. Kerth, W. A. Wenzel, and T. F. Zipf, Phys. Rev. 123, 320 (1961); O. Chamberlain, K. M. Crowe, D. Keefe, L. T. Kerth, A. Lemonick, T. Maung, and T. F. Zipf, Phys. Rev. 125, 1696 (1962).

2. A. Barbaro-Galtieri, A. Hussain, and R. D. Tripp, Phys. Letters 6, 296 (1963).

3. E. F. Beall, W. Holley, D. Keefe, L. T. Kerth, J. J. Thresher, C. L. Wang, and W. A. Wenzel, Elastic K^-p Scattering Between 700 and 1400 MeV/c, in Proceedings of the 1962 International Conference on High-Energy Physics at CERN, edited by J. Prentki (CERN, Scientific Information Service, Geneva, 1962), p. 368; L. A. Sodickson, I. Manelli, M. Wahlig, and D. Frisch, Phys. Rev. 133, B757 (1964); W. Graziano and S. G. Wojcicki, Phys. Rev. 128, 1868 (1962); P. L. Bastien and J. P. Berge, Phys. Rev. Letters 10, 188 (1963); C. Wohl, M. H. Alston, G. R. Kalbfleisch, D. H. Miller, and S. G. Wojcicki, Bull. Am. Phys. Soc. 8, 341 (1963).

4. W. M. Smart, Study of the Y_1^* Resonant Amplitudes Between 1660 and 1900 MeV in the Reaction $K^-n \rightarrow \Lambda \pi^-$ (Ph.D. Thesis), Lawrence Radiation Laboratory Report UCRL-17712, August 1967 (unpublished); see also W. M. Smart, A. Kernan, G. E. Kalmus, and R. P. Ely, Jr., Phys. Rev. Letters 17, 556 (1966).

5. R. B. Bell, R. W. Bland, M. G. Bowler, J. L. Brown, R. P. Ely, S. Y. Fung, G. Goldhaber, A. A. Hirata, J. A. Kadyk, J. Louie, J. S. Sahouria, V. H. Seeger, W. M. Smart, G. H. Trilling, and C. T. Murphy, A Variable Momentum Separated $K^\pm$ Beam at the Bevatron, in Proceedings of the XIIth International Conference on High Energy Physics, Dubna, 1964 (Atomizdat, Moscow, 1966), Vol. I, p. 546.

6. J. V. Franck, P. V. C. Hough, and B. W. Powell, Nucl. Instr. Methods 20, 387 (1963); M. Alston, J. V. Franck, and L. T. Kerth, Conventional and Semiautomatic Data Processing and Interpretation, in Bubble and Spark Chambers, edited by R. P. Shutt (Academic Press, New York, 1967), Vol. II, Ch. 2.

7. H. S. White, S. S. Buckman, D. E. Hall, E. Hurwitz, L. B. Meissner, J. C. Smith, and F. R. Stannard, The FOG, CLOUDY, and FAIR Programs for Bubble Chamber Data Reduction, Lawrence Radiation Laboratory Report UCRL-9457, August 1960 (unpublished).

8. Later independent and thorough examinations of procedure and of previously unused τ's, and using the new beam count, gave branching ratios of (5.46±0.22)% for 2546 τ's and (5.71±0.22)% for 3273 τ's, both consistent with the current figure[11] of (5.57±0.04)%. J. S. Sahouria and W. Press (Powell-Birge Group, Lawrence Radiation Laboratory), private communications, June and December 1966.

9. B. Rossi, High Energy Particles (Prentice-Hall, New Jersey, 1952), Ch. 2; F. Crawford, Use of Delta Rays to Determine Particle Velocities, Lawrence Radiation Laboratory Alvarez Group Note UCID-241, November 1957 (unpublished).

10. J. L. Brown, Theoretical Index of Refraction in Various Hydrogen/Deuterium Experiments, Lawrence Radiation Laboratory Trilling-Goldhaber Group Note TGT-25, October 1964 (unpublished).

11. A. H. Rosenfeld, N. Barash-Schmidt, A. Barbaro-Galtieri, L. R. Price, M. Roos, P. Söding, W. J. Willis, and C. G. Wohl, Rev. Mod. Phys. 40, 77 (1968).

12. M. S. Bartlett, Phil. Mag. 44, 249 (1953); J. Louie, Lambda Lifetime and Bartlett S-Function Technique, Lawrence Radiation Laboratory Powell-Birge Group Note PB-104, December 1966 (unpublished).

13. A study has shown that systematic discrepancies in FSD-measured origins are exponentially distributed with a mean of 1.9±0.1 mm, with a corresponding value of about 0.4 mm for Franckenstein-measured events. W. Press (Powell-Birge Group, Lawrence Radiation Laboratory), private communication, Summer 1966.

14. G. T. Hoff, Phys. Rev. 131, 1302 (1963); Phys. Rev. 139, B671 (1965).

15. A. Kanazawa, Phys. Rev. 123, 997 (1961).

16. L. E. Evans and J. M. Knight, Phys. Rev. 137, B1232 (1965).

17. W. G. Holladay, Poles and Resonances in the Process $\pi^+ + p \rightarrow \Sigma^+ + K^+$, in Proceedings of the Second Topical Conference on Resonant Particles, Ohio University, Athens, 1965, edited by B. A. Munir (Ohio University, Athens, 1965), p. 72.

18. M. L. Stevenson, Evidence for a T=1, $J^P=7/2^+$ Hyperon Resonance at 2050 MeV, Invited Paper, Am. Phys. Soc. Meeting, U.C.L.A., December 1965.

19. S. Minami, Phys. Letters 24B, 188 (1967).

20. G. F. Chew, M. L. Goldberger, F. E. Low, and Y. Nambu, Phys. Rev. 106, 1337 (1967); J. D. Bjorken and S. D. Drell, Relativistic Quantum Mechanics (McGraw-Hill, New York, 1964); H. Pilkuhn, The Interactions of Hadrons (North-Holland, Amsterdam, 1967).

21. R. D. Tripp, Baryon Resonances, in Proceedings of the International School of Physics "Enrico Fermi", Course 33 (Academic Press, New York, 1966), p. 70.

22. S. L. Glashow and A. H. Rosenfeld, Phys. Rev. Letters 10, 192 (1963).

23. Bateman Manuscript Project, Higher Transcendental Functions, edited by A. Erdélyi (McGraw-Hill, New York, 1953), Vol I, Ch. 3.

24. E. Jahnke and F. Emde, Tables of Functions with Formulae and Curves (Dover Publications, New York, 1945).

25. R. Armenteros, M. Ferro-Luzzi, D. W. G. Leith, R. Levi-Setti, A. Minten, R. D. Tripp, H. Filthuth, V. Hepp, E. Kluge, H. Schneider, R. Barloutaud, P. Granet, J. Meyer, J. P. Porte, Nucl. Phys. (to be published).

26. R. W. Birge, R. P. Ely, G. E. Kalmus, A. Kernan, J. Louie, J. S. Sahouria, and W. M. Smart, The Spin and Parity of the $Y_0^*(1815)$ and the $Y_1^*(1765)$, in Proceedings of the Second Topical Conference on Resonant Particles, Ohio University, Athens, 1965, edited by B. A. Munir (Ohio University, Athens, 1965), p. 296.

27. Reference 11 lists $\alpha_\Lambda = 0.647 \pm 0.016$. Our value of 0.66 was taken from their preceding compilation, Rev. Mod. Phys. 39, 1 (1967).

28. See, for example, F. T. Solmitz, Ann. Rev. Nucl. Sci. 14, 375 (1964).

29. E. R. Beals, ZO BKY VARMIT, Lawrence Radiation Laboratory Computer Center Library Note, June 1966 (unpublished). See also reference 4.

30. W. C. Davidon, Variable Metric Method for Minimization, Argonne National Laboratory Report ANL-5990 Rev., November 1959 (unpublished).

31. L. W. Alvarez, M. H. Alston, M. Ferro-Luzzi, D. O. Huwe, G. R. Kalbfleisch, D. H. Miller, J. J. Murray, A. H. Rosenfeld, J. B. Shafer, F. T. Solmitz, and S. G. Wojcicki, Phys. Rev. Letters 10, 184 (1963); P. L. Bastien, K^--Proton Interactions Near 760 MeV/c (Ph. D. Thesis), Lawrence Radiation Laboratory Report UCRL-10779, February 1963 (unpublished); G. W. London, R. R. Rau, N. P. Samios, S. S. Yamamoto, M. Goldberg, S. Lichtman, M. Prime, and J. Leitner, Phys. Rev. 143, 1034 (1966).

32. R. L. Cool, G. Giacomelli, T. F. Kycia, B. A. Leontić, K. K. Li, A. Lundby, and J. Teiger, Phys. Rev. Letters 16, 1228 (1966).

33. J. D. Davies, J. D. Dowell, P. M. Hattersley, R. J. Homer, A. W. O'Dell, A. A. Carter, K. F. Riley, R. J. Tapper, D. V. Bugg, R. S. Gilmore, K. M. Knight, D. C. Salter, G. H. Stafford, and E. J. N. Wilson, Phys. Rev. Letters 18, 62 (1967).

34. C. G. Wohl, F. T. Solmitz, and M. L. Stevenson, Phys. Rev. Letters 17, 107 (1966).

35. W. M. Smart, Phys. Rev. 169, 1330 (1968).

36. J. J. de Swart, Rev. Mod. Phys. 35, 916 (1963).

37. A. Scotti and D. Y. Wong, Phys. Rev. 138, B145 (1965).

38. M. Gell-Mann and F. Zachariasen, Phys. Rev. 124, 953 (1961).

39. A. W. Martin and K. C. Wali, Phys. Rev. 130, 2455 (1963).

40. J. J. Sakurai, Nuovo Cimento 34, 1582 (1964).

41. J. D. Jackson and H. Pilkuhn, Nuovo Cimento 33, 906 (1964).

42. R. L. Warnock and G. Frye, Phys. Rev. 138, B947 (1965).

43. C. H. Chan and F. T. Meiere, Phys. Rev. Letters 20, 568 (1968).

44. J. D. Jackson, J. T. Donohue, K. Gottfried, R. Keyser, and B. E. Y. Svensson, Phys. Rev. 139, B428 (1965).

45. N. M. Gelfand, D. Harmsen, R. Levi-Setti, E. Predazzi, M. Raymund, J. Doede, and W. Männer, Phys. Rev. Letters 17, 1224 (1966).

46. D. V. Bugg, R. S. Gilmore, K. M. Knight, D. C. Salter, G. H. Stafford, E. J.N. Wilson, J. D. Davies, J. D. Dowell, P. M. Hattersley, R. J. Homer, A. W. O'Dell, A. A. Carter, R. J. Tapper, and K. F. Riley, Phys. Rev. 168, 1466 (1968).

47. K. Gottfried and J. D. Jackson, Nuovo Cimento 34, 735 (1964). The estimate comes from the data of the Aachen-Birmingham-Bonn-Hamburg-London-München Collaboration, Nuovo Cimento 31, 729 (1964).

48. C. Schmid, Phys. Rev. Letters 20, 689 (1968).

49. P. D. B. Collins, R. C. Johnson, and E. J. Squires, Phys. Letters 27B, 23 (1968).

FIGURE CAPTIONS

Fig. 1. Schematic of the beam line.

Fig. 2. Example of a 0-prong+V in the chamber.

Fig. 3. Lateral deviations, Δy, of beam tracks (A) toward the beginning and (B) toward the end of Roll 2201. Tracks falling between ± 1.2 cm were accepted.

Fig. 4A. A kinematic ellipse plot for $K^- + p \rightarrow \Lambda + \pi^0$. The semi-minor axis is the final-state c.m. momentum, and the distance between the Λ vertex at the left and the π^0 vertex at the right is equal to the K^- lab momentum. Lab momenta and angles for various c.m. cosines at the perimeter may be read off directly: Λ (π^0) in the upper (lower) half-plane.

Fig. 4B. A similar plot for $K^- + p \rightarrow \bar{K}^0 + n$. Quantities for the n ($\bar{K}^0$) are in the upper (lower) half-plane.

Fig. 5A. Curves of constant decay opening angle between the decay products for K_1^0 and Λ. The lab momentum of the (-) decay product is plotted against that of the (+) decay product.

Fig. 5B. The expected isotropic distribution of the π^- in the K_1^0 c.m.; the Λ events which simulate K_1^0 show up in the backward angles. The lower histogram shows the K_1^0's separated from the Λ's.

Fig. 6A Positions of the production vertex along the chamber. The entrance to the chamber is located at x=24 cm.

Fig. 6B. Lateral positions of the decay vertices along the beam. Events falling outside a radius of 21.5 cm from (x,y)=(48.5,50) cm were rejected.

Fig. 7A. Length of the Λ before decaying. A cutoff length L_o=0.8 cm was used.

Fig. 7B. Histogram of W_L, the weight for the Λ length selection assigned to events meeting the fiducial, length, and missing-mass-squared criteria. The limit near W_L=1.1 is due to the kinematics of the problem and to the non-zero cutoff length.

Fig. 8A. Azimuthal distribution for high momentum Λ's.

Fig. 8B. The same distribution for low momentum Λ's. Losses of Λ's whose momenta make small angles with respect to the camera axis would be evident near φ=90° and 270°.

Fig. 9. The combined distribution of the square of the missing mass of neutrals recoiling against the Λ for events satisfying the fiducial and length criteria.

Fig. 10A. Angular distribution of the π^0 at p_K=1019 MeV/c for events satisfying fiducial and length criteria (lower histogram). The distribution for events weighted by W_m alone is shown as the upper histogram.

Fig. 10B. Distribution of χ^2 for the 1C-fit for events meeting the fiducial, length, and missing-mass-squared criteria.

Fig. 11. Complex T-plane with unitary bounds for a resonant state (small circles). The circle centered at the origin with radius 0.5 is the limit for partial-wave amplitudes in a reaction channel. These limits are drawn for partial-wave amplitudes in a state of pure isotopic spin.

Fig. 12. Cross sections for $K^- + p \rightarrow \Lambda + \pi^0$. The solid curve fit to the data points in the present experiment are from solution 16. The points of Armenteros et al.[27] are also plotted.

Fig. 13. Production angular distributions of the π^0 for $K^- + p \rightarrow \Lambda + \pi^0$. The solid curves are the fit to our data from solution 16.

Fig. 14. The Λ polarization for our experiment. The solid curves show the fit to the data from solution 16.

Fig. 15A. Plot for solution 5a of the D5, F5, F7, and D3 resonant amplitudes with real t- and u-channel exchange projections is a fit to the data shown in Figs. 12-14. The (+) symbols denote the excursion limits of the amplitudes over our energy range.

Fig. 15B. Plot for solution 14 of the same resonant amplitudes but with a t-channel exchange modified by a phase factor.

Fig. 15C. Plot for solution 16 of the same resonant amplitudes with both t- and u-channel terms modified by phase factors.

Fig. 16. Plot for solution 15 showing D5, F7, and D3 resonant amplitudes; both t- and u-channel terms have been modified by phase factors.